

# Robustness via Deep Low-Rank Representations

Amartya Sanyal<sup>\*1,2</sup>, Varun Kanade<sup>1,2</sup>, Philip HS Torr<sup>3</sup>, and Puneet K Dokania<sup>3</sup>

<sup>1</sup>Department of Computer Science, University of Oxford

<sup>3</sup>Department of Engineering Science, University of Oxford

<sup>2</sup>The Alan Turing Institute, London.

## Abstract

We investigate the effect of the dimensionality of the representations learned in Deep Neural Networks (DNNs) on their robustness to input perturbations, both adversarial and random. To achieve low dimensionality of learned representations, we propose an easy-to-use, end-to-end trainable, low-rank regularizer (LR) that can be applied to any intermediate layer representation of a DNN. This regularizer forces the feature representations to (mostly) lie in a low-dimensional linear subspace. We perform a wide range of experiments that demonstrate that the LR indeed induces low rank on the representations, while providing modest improvements to accuracy as an added benefit. Furthermore, the learned features make the trained model significantly more robust to input perturbations such as Gaussian and adversarial noise (even without adversarial training). Lastly, the low-dimensionality means that the learned features are highly compressible; thus discriminative features of the data can be stored using very little memory. Our experiments indicate that models trained using the LR learn robust classifiers by discovering subspaces that avoid non-robust features. Algorithmically, the LR is scalable, generic, and straightforward to implement into existing deep learning frameworks.

## 1 Introduction

Dimensionality reduction methods are some of the oldest techniques in machine learning that extract a small number of factors from a dataset that explain the most of its variance; these factors contain most of the *discriminative* power useful in classification or regression tasks, and are known to increase *robustness*, i.e. these methods typically have a denoising effect. Perhaps, the most popular and widely used among them are PCA (see e.g. (Jolliffe, 2002)) and CCA (Hotelling, 1935).

In recent years, deep neural networks (DNNs) have proved to be the state-of-the-art models for a wide range of tasks. An intriguing aspect has been their ability to generate representations directly from raw data that are useful in several tasks, including ones for which they were not specifically trained, usually known as *representation learning* (Zeiler & Fergus, 2014; Sermanet et al., 2014; Donahue et al., 2014). Essentially, for most models trained in a supervised fashion, the vector of activations in the penultimate layer is a *learned* representation of the raw input. The remarkable success of DNNs is primarily attributed to the discriminative quality of this learned representation space. However, despite their impressive performance, DNNs are known to be brittle to input perturbations (Szegedy et al., 2013; Goodfellow et al., 2014). This raises concerns regarding the robustness of the factors captured by the learned representation space of DNNs. As mentioned earlier, the factors captured by dimensionality reduction techniques, while being discriminative, are robust to input perturbations. This motivates the thesis behind this work—if we enforce DNNs to learn representations that lie in a low-dimensional subspace (for the entire dataset), we would obtain more robust classifiers while preserving their discriminative power.

Ideally, to encourage learning low-dimensional representations, we would like to insert a *dimensionality reduction* “module” in DNNs and develop an end-to-end training method that simultaneously does supervised

---

\*amartya.sanyal@cs.ox.ac.uk

training and dimensionality reduction. At first glance, using SVD to project representations into lower dimensional subspace seems viable. However, this approach encounters challenges because of the large number of training examples, and, also due to the fact that the representations themselves change after every parameter update (discussed later in detail). A workaround could be to design architectures with bottlenecks similar to auto-encoders (Hinton & Salakhutdinov, 2006). The fact that most of the state-of-the-art networks do not have such bottlenecks limit their usability.

Our work provides the benefits of dimensionality reduction by inserting a *virtual layer* (not used at prediction time) and augmenting the loss function to induce low-rank representations. Precisely, we propose a low-rank Regularizer (LR) that (1) does not put any restriction on the network architecture,<sup>1</sup> (2) is end-to-end trainable, and (3) is efficient in that it allows mini-batch training. LR explicitly *enforces* representations to lie in a linear subspace with low *intrinsic* dimension and is guaranteed to provide low-rank representations for the entire dataset even when trained using mini batches. As LR is a virtual layer, it can be applied to any intermediate representations of DNNs. It is sensible to do so as, DNNs, actually learn hierarchical representations, one after another. These intermediate representations are known to capture interesting properties such as semantic meaning or concepts needed to improve the discriminative power of the penultimate layer representation.

Apart from successfully reducing the dimensionality of learned representations, DNNs trained with LR turn out to be significantly more robust to input perturbations, both adversarial and random, while providing modest improvements over the unperturbed test accuracy. This is of particular interest as it suggests that adding well-thought priors over factors influencing the representation space (e.g. low-rank prior over representations) might further improve the robustness of DNNs, before *actually* reaching the limit beyond which robustness comes at a cost, be it computational (Goodfellow et al., 2014; Madry et al., 2018), statistical (Schmidt et al., 2018) or a loss in accuracy (Tsipras et al., 2019).

Lastly, because of the low-dimensionality, we are able to compress representations by a significant factor without losing its discriminative power. Thus, discriminative features of the data can be stored using very little memory. For example, we show in one of our experiments that, even with a 5-dimensional embedding (400x compression), the model with LR loses only 6% in accuracy.

## 2 Deep Low-Rank Representations

Consider  $f : \mathbb{R}^p \mapsto \mathbb{R}^k$  to be a feed-forward multilayer NN that maps  $p$  dimensional input  $\mathbf{x}$  to a  $k$  dimensional output  $\mathbf{y}$ . We can decompose this into two sub-networks, one consisting of the layers before the  $\ell^{\text{th}}$  layer and one after i.e.  $f(\mathbf{x}) = f_{\ell}^{+}(f_{\ell}^{-}(\mathbf{x}; \phi); \theta)$ , where  $f_{\ell}^{-}(\cdot; \phi)$ , parameterized by  $\phi$ , represents the part of the network up to layer  $\ell$  and,  $f_{\ell}^{+}(\cdot; \theta)$  represents the part of the network thereafter. With this notation, the  $m$  dimensional representation (or the activations) of any layer  $\ell$  can simply be written as  $\mathbf{a} = f_{\ell}^{-}(\mathbf{x}; \phi) \in \mathbb{R}^m$ . In what follows, we first formalize the low-rank representation problem, then provide insights on its difficulty, and finally propose our approach to solve it approximately and efficiently.

**Problem Formulation:** Let  $\mathbf{X} = \{\mathbf{x}_i\}_{i=1}^n$  and  $\mathbf{Y} = \{\mathbf{y}_i\}_{i=1}^n$  be the set of inputs and outputs of a given training dataset. By slight abuse of notation, we define  $\mathbf{A}_{\ell} = f_{\ell}^{-}(\mathbf{X}; \phi) = [\mathbf{a}_1, \dots, \mathbf{a}_n]^{\top} \in \mathbb{R}^{n \times m}$  to be the activation matrix of the entire dataset, so that  $\mathbf{a}_i$  is the activation vector of the  $i$ -th sample. Note that for most practical purposes  $n \gg m$ . In this setting, the problem of learning low-rank representations can be formulated as a constrained optimization problem as follows:

$$\min_{\theta, \phi} \mathcal{L}(\mathbf{X}, \mathbf{Y}; \theta, \phi), \text{ s.t. } \text{rank}(\mathbf{A}_{\ell}) = r, \quad (1)$$

where  $\mathcal{L}(\cdot)$  is the loss function and  $r < m$  is the desired rank of the representations at layer  $\ell$ . The rank  $r$  is a hyperparameter (though empirically not a sensitive one as observed in our experiments). Throughout this section, we consider imposing low-rank constraints over only one intermediate layer, however, the methods provided here can be easily extended to any number of layers. Note that both the loss and the constraint set of the above objective function are non-convex. One approach to optimize this would be to perform alternate

---

<sup>1</sup>It puts no *direct* restriction, though of course any extra regularization will produce an inductive bias.

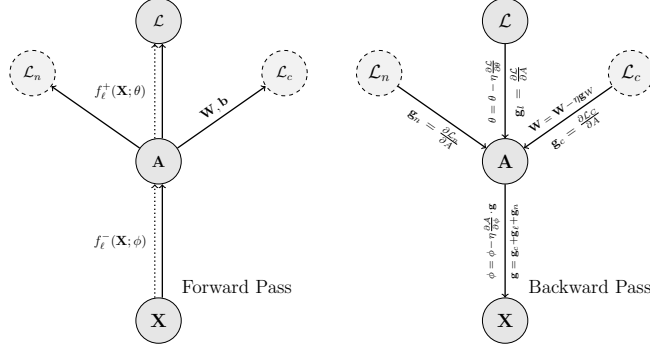


Figure 1: **The LR layer.** Left figure shows the *forward pass*, *solid edges* show the flow of data during training, *dashed edges* show the flow of data during inference, and *dashed nodes* indicate the *virtual layer*. Right figure shows the *backward pass*.

minimization, first over the loss (gradient descent) and then projecting onto the non-convex set to satisfy the rank constraint.

Since  $n \gg m$ , ensuring  $\text{rank}(\mathbf{A}_\ell) = r$  would be practically infeasible as it would require performing SVD at every iteration (at cost  $\mathcal{O}(n^2m)$ ). A feasible, but incorrect, approach would be to do this on mini-batches, instead of the entire dataset. However, projecting each mini-batch onto the space of rank  $r$  matrices does not guarantee that the activation matrix of the entire dataset will be of rank  $r$ , as each of these mini-batches can lie in very different subspaces. Computational issues aside, another crucial problem stems from the fact that the activation matrix  $\mathbf{A}_\ell = f_\ell^-(\cdot; \phi)$  is itself parameterized by  $\phi$  and thus  $\phi$  needs to be updated in a way such that the generated  $\mathbf{A}_\ell$  is low rank and it is not immediately clear how to use the low-rank projection of  $\mathbf{A}_\ell$  to achieve this. One might suggest to first fully train the network and then obtain low rank projections of the activations. However, as our experiments show, this procedure does not provide the two main benefits: compression and robustness.

**Low-Rank Regularizer:** We now describe our regularizer that encourages learning low-rank activations, and, if optimized properly, guarantees that the rank of the activation matrix (of any size) will be bounded by  $r$ . We do this by introducing an auxiliary parameter  $\mathbf{W} \in \mathbb{R}^{m \times m}$ , augmenting the loss function and shifting the low-rank constraint from the activation matrix  $\mathbf{A}_\ell$  (as in (1)) to this auxiliary parameter  $\mathbf{W}$ . Switching the rank constraint to  $\mathbf{W}$  has two advantages: The rank constraint is put (a) on a matrix that is independent of the batch/dataset size, and (b) on a parameter as opposed to a data-dependant intermediate tensor (like activations), and can thus be updated directly at each iteration. Combining these ideas, our final augmented objective function, with the regularizer, is as follows:

$$\begin{aligned} \min_{\theta, \phi, \mathbf{W}, \mathbf{b}} \quad & \mathcal{L}(\mathbf{X}, \mathbf{Y}; \theta, \phi) + \mathcal{L}_c(\mathbf{A}_\ell; \mathbf{W}, \mathbf{b}) + \mathcal{L}_n(\mathbf{A}_\ell) \\ \text{s.t.} \quad & \mathbf{W} \in \mathbb{R}^{m \times m}, \text{rank}(\mathbf{W}) = r, \mathbf{b} \in \mathbb{R}^m, \mathbf{A} = f_\ell^-(\mathbf{X}; \phi), \end{aligned} \quad (2)$$

where,

$$\begin{aligned} \mathcal{L}_c(\mathbf{A}; \mathbf{W}, \mathbf{b}) &= \frac{1}{n} \sum_{i=1}^n \left\| \mathbf{W}^\top (\mathbf{a}_i + \mathbf{b}) - (\mathbf{a}_i + \mathbf{b}) \right\|_2^2, \\ \text{and } \mathcal{L}_n(\mathbf{A}) &= \frac{1}{n} \sum_{i=1}^n \left| 1 - \|\mathbf{a}_i\| \right|. \end{aligned}$$

The intuition behind our approach is that we add a virtual (doesn't modify the main network) branch at layer  $\ell$ , the goal of which is to learn a low-rank identity projection for  $\mathbf{A}_\ell$ . It is well known that for a low-rank matrix, there exists a low-rank projection that projects the matrix onto itself<sup>2</sup>. Thus, if such a

<sup>2</sup>It is the PCA problem

low-rank identity map does not exist for  $\mathbf{A}_\ell$  i.e.  $\mathbf{A}_\ell$  is not low-rank, then the goal of our regularizer is to jointly penalize the activations to make them low-rank and learn that low-rank identity map.

Specifically, minimizing the projection loss  $\mathcal{L}_c$  ensures that the affine low-rank mappings ( $\mathbf{AW}$ ) of the activations are close to the original ones i.e.  $\mathbf{AW} \approx \mathbf{A}$ . As  $\mathbf{W}$  is low-rank,  $\mathbf{AW}$  is also low-rank and thus implicitly (due to  $\mathbf{AW} \approx \mathbf{A}$ ) it forces the original activations  $\mathbf{A}$  to be low-rank. The bias  $\mathbf{b}$  allows for the activations to be translated before projection.<sup>3</sup> However note that setting  $\mathbf{A}$  and  $\mathbf{b}$  close to zero trivially minimizes  $\mathcal{L}_c$ , especially when the activation dimension is large. We observed this to happen in practice as it is easier for the network to learn  $\phi$  such that the activations and the bias are very small in order to minimize  $\mathcal{L}_c$ . To prevent this, we use  $\mathcal{L}_n$  that acts as a norm constraint on the activation vector to keep the activations sufficiently large. Lastly, as the rank constraint is now over  $\mathbf{W}$  and  $\mathbf{W}$  is a *global* parameter independent of the dimension  $n$  (i.e. size of minibatch/dataset) we can use mini-batches to optimize (2). Since  $\text{rank}(\mathbf{AW}) \leq r$  for any  $\mathbf{A}$ , optimizing over mini-batches still ensures that the entire activation matrix is low-rank. Intuitively, this is due to the fact that the basis vectors of the low-rank affine subspace are now captured by the low-rank parameter  $\mathbf{W}$ . Thus, as long as  $\mathcal{L}_c$  is minimized for all the mini-batches,  $\mathbf{A} \approx \mathbf{AW}$  holds for the entire dataset, leading to the low-dimensional support.

---

**Algorithm 1** Low-Rank (LR) Regularizer

---

**input** Activation Matrix  $\mathbf{A}_l$ , gradient input  $\mathbf{g}_l$

- 1:  $\mathbf{Z} \leftarrow (\mathbf{A}_l + \mathbf{b})^\top \mathbf{W}^4$  {forward propagation towards the virtual LR layer}
  - 2:  $\mathcal{L}_c \leftarrow \frac{1}{b} \|\mathbf{Z} - (\mathbf{A}_l + \mathbf{b})\|_2^2$  {the reconstruction loss}
  - 3:  $\mathcal{L}_n \leftarrow \frac{1}{b} \sum_{i=1}^b |\mathbf{1} - \|\mathbf{a}_i\||$  {norm constraint loss}
  - 4:  $\mathbf{g}_W \leftarrow \frac{\partial \mathcal{L}_c}{\partial \mathbf{W}}$ ,  $\mathbf{g} \leftarrow \mathbf{g}_l + \frac{1}{b} \sum_{i=1}^b \frac{\partial (\mathcal{L}_c + \mathcal{L}_n)}{\partial \mathbf{a}_i}$
  - 5:  $\mathbf{W} \leftarrow \mathbf{W} - \lambda \mathbf{g}_W$
  - 6:  $\mathbf{W} \leftarrow \Pi_k^{\text{rank}}(\mathbf{W})$  {hard thresholds the rank of  $\mathbf{W}$ }
- output**  $\mathbf{g}$  {the gradient to be passed to the layer before}
- 

**Implementing the Low-Rank Regularizer:** Algorithm 1 (further details in Appendix B.1) describes the forward and the backward operations of the low-rank virtual layer for a mini-batch of size  $b$ . We present a flow diagram for the same in Figure 1. This layer is virtual in the sense that it only includes the parameters  $\mathbf{W}$  and  $\mathbf{b}$  that are not used in the NN model itself to make predictions, but nonetheless the corresponding loss term  $\mathcal{L}_c$  does affect the model parameters through gradient updates. Algorithm 1 alternately minimizes the augmented loss function (Line 1-5) and projects the auxiliary parameter  $\mathbf{W}$  to the space of low-rank matrices. The algorithm is reminiscent of the Singular Value Projection (SVP) Algorithm (Jain et al., 2010). However, to make the algorithm practical for high dimensional representation spaces, we use ensembled Nyström SVD (Williams & Seeger, 2001; Halko et al., 2011; Kumar et al., 2009a) for the projection in Step 6 (details in Appendix B).

### 3 Experiments

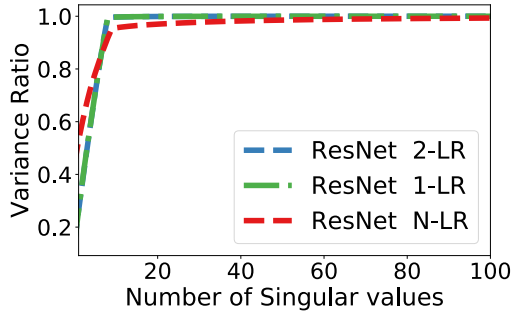
We perform a wide range of experiments to show the effectiveness of imposing low-rank constraints on the representations of a dataset using our proposed LR. Briefly,

- We show that LR indeed reduces the rank of the representation space and improves robustness for both, *adversarial* and *random* noise input perturbations, while providing modest improvements over accuracy.
- We show results on both, white-box and black-box adversarial attacks.
- In addition, we compare LR with various different approaches such as Stable Rank Normalization (Sanyal et al., 2020), Pruning (Lee et al., 2019), and Spectral Normalization (Miyato et al., 2018) where the parameter space, instead of the activations, is being either compressed or encouraged to have low *effective* rank.

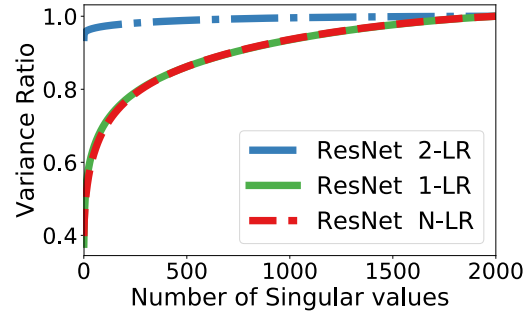
---

<sup>3</sup>We use the term *projection* loosely as we do not strictly constrain  $\mathbf{W}$  to be a projection matrix.

<sup>4</sup> $\mathbf{A} + \mathbf{b}$  is computed by adding  $\mathbf{b}$  to every row in  $\mathbf{A}$



(a) CIFAR10: Activations after last ResNet block.



(b) CIFAR10: Activations before last ResNet block

Figure 2: Variance Ratio captured by varying number of Singular Values

- Lastly, we provide analyses to show that the representations learned using LR is extremely discriminative and, because they lie in a linear space with low *intrinsic* dimension, can be compressed significantly.

**Architectures and Datasets** We use the standard ResNet (He et al., 2016) architecture with four residual blocks. To capture the effect of network depth, we use ResNet-50 (R50) and ResNet-18 (R18). Since LR can be applied to any representation layer in the network, we investigate the following two configurations:

- **1-LR**, where the LR layer is located just before the last fully-connected (FC) layer that contains 512 and 2048 units in ResNet-18 and ResNet-50, respectively.
- **2-LR**, where there are two LR layers, the first one positioned before the fourth ResNet block with 16,384 incoming units, and the second one just before the FC layer as in ResNet 1-LR.
- **N-LR**, without any LR layer (standard setting).

Other model formulations that we consider such as *bottle-LR* and *hybrid max-margin* models will be discussed when introduced. We use CIFAR10 and CIFAR100 datasets and show results using the coarse labels (20 classes) of CIFAR100. Further experimental details and additional experiments on other models (VGG19) and datasets (CIFAR100 with fine labels and SVHN) are reported in Appendix C. Experimentally we observed that the target rank is not a sensitive hyper-parameter, as the training enforces a much lower rank than what it is set to. For our experiments, we set a target rank of 100 for the layer before the last FC layer and 500 for the layer before the fourth ResNet block.

**Effective Rank** Before we discuss our primary findings, here we empirically show the effect of LR on the effective rank of activations. We use the standard *variance ratio*, defined as  $\sum_{i=1}^r \sigma_i^2 / \sum_{i=1}^p \sigma_i^2$ , where  $\sigma_i$ 's are the ordered singular values of the given activation matrix  $A$ ,  $p$  is the rank of the matrix, and  $r \leq p$ . Given  $r$ , a higher value of variance ratio indicates that a larger fraction of the total variance in the data is captured in the  $r$  dimensional subspace.

Fig. 2(a) shows the variance ratio for the activations before the last FC layer. Note that even for NLR, the effective rank is as low as 10. Similar low-rank structure was also observed empirically by Oyallon (2017). However, the LR-models have almost negligible variance leakage.

Fig. 2(b) shows the variance ratio for the activations before the 4th ResNet block. The activation vector is 16,384-dimensional and the use of the Nyström method ensures computational feasibility. Note, ResNet 2-LR is the only model that has an LR-layer in that position and these figures show that *2-LR is the only model that shows a (reasonably) low-rank structure on that layer*. More experiments provided in the Appendix (Fig 5 and Figs. 6(a), 6(b)).

### 3.1 Adversarial Robustness

We now begin our analysis on the impact of low-rank representations on adversarial robustness. We would like to highlight that in all our experiments, all the models are trained using clean dataset. This is important as it shows whether training on clean dataset, with well-thought priors or regularizers, can actually improve adversarial robustness without compromising with the clean data test accuracy. We recall that adversarial

		Adversarial Test Accuracy(%)								Clean Test Accuracy (%)		
		$L_\infty$ radius	8/255		10/255		16/255		20/255			
		Attack iterations	7	20	7	20	7	20	7	20		
White Box	C10	R50	N-LR	43.1	31.0	38.5	21.8	31.2	7.8	28.9	4.5	<b>95.4</b>
			1-LR	<b>79.1</b>	<b>78.5</b>	<b>78.6</b>	<b>78.1</b>	<b>77.9</b>	<b>77.0</b>	<b>77.1</b>	<b>76.6</b>	<b>95.4</b>
		R18	N-LR	40.9	26.7	35.1	16.6	26.7	4.4	24.3	2.3	94.6
			1-LR	48	31.3	44.4	25.4	39.6	17.9	38.2	15.7	<b>94.9</b>
			2-LR	<b>54.7</b>	<b>37.6</b>	<b>52.4</b>	<b>33.1</b>	<b>48.7</b>	<b>25.7</b>	<b>48.0</b>	<b>23.6</b>	94.5
	C100	R50	N-LR	37.2	29.9	34.1	24.6	29.8	15.9	34.1	13.3	<b>85.8</b>
			1-LR	<b>45.3</b>	<b>38.7</b>	<b>43.7</b>	<b>35.8</b>	<b>40.9</b>	<b>31.5</b>	<b>40.0</b>	<b>29.8</b>	<b>85.8</b>
		R18	N-LR	30.6	23.2	26.4	16.9	20.5	7.42	18.4	5.1	84.1
			1-LR	<b>34.5</b>	<b>25.4</b>	<b>31.3</b>	<b>20.2</b>	<b>27.3</b>	<b>13.1</b>	<b>25.7</b>	<b>10.8</b>	<b>84.2</b>
			2-LR	33.82	24.37	30.9	19.1	26.8	11.83	25.41	9.9	84
Black Box	C10	R50	1-LR	64.7	56.8	59.0	47.5	51.2	28.0	48.3	20.6	95.4
		R18	1-LR	66.6	60.8	61.1	51.0	52.2	31.52	49.8	23.6	94.9
			2-LR	68.0	62.5	62.3	53.4	53.8	33.5	50.8	25.8	94.5
		C100	R50	1-LR	52.4	46.2	48.1	38.8	42.0	25.4	48.1	20.9
	R18		1-LR	53.0	48.6	47.9	41.0	41.1	26.3	38.7	20.4	84.2
			2-LR	51.3	47.2	46.9	39.9	39.5	24.3	37.2	19.2	84

Table 1: Adversarial Test Accuracy against a  $\ell_\infty$  constrained PGD adversary with the  $\ell_\infty$  radius bounded by  $\epsilon$  and the number of attack steps bounded by  $\tau$ . R50 and R18 denotes ResNet50 and ResNet18 respectively. C10 and C100 refer to CIFAR10 and CIFAR100 (Coarse labels) respectively.

		Adversarial Acc.(%)				Test			
$L_\infty$ radius	Att. iter	8/255		10/255		16/255		20/255	
		7	20	7	20	7	20	7	20
N-LR		43.1	31.0	38.5	21.8	31.2	7.8	28.9	4.5
SNIP		29.4	14.5	25.0	8.0	18.5	1.3	16.2	0.4
SRN		47.8	37.6	44.4	31.4	39.8	21.3	37.5	18.4
SN		54.2	43.8	50.8	36.4	45.0	22.6	42.8	18.1
LR (Ours)		<b>79.1</b>	<b>78.5</b>	<b>78.6</b>	<b>78.1</b>	<b>77.9</b>	<b>77.0</b>	<b>77.1</b>	<b>76.6</b>

Table 2: Robustness of other regularization/compression techniques to Adversarial Perturbations.

perturbations are well crafted (almost imperceptible) input perturbations that, when added to a clean input, flips the prediction of the model on the input to an incorrect one Szegedy et al. (2013). Various methods (Szegedy et al., 2013; Goodfellow et al., 2014; Kurakin et al., 2017; Moosavi-Dezfooli et al., 2016) have been proposed in recent years for constructing adversarial perturbations.

Here we use the following three **white-box** adversarial attacks to perform our experiments:

1. Iterative Fast Sign Gradient Method (Iter-FSGM or IFSGM) (Kurakin et al., 2016; Madry et al., 2018),
2. Iterative Least Likely Class Method (Iter-LL-FSGM or ILL) (Kurakin et al., 2017), and
3. DeepFool (DFL) (Moosavi-Dezfooli et al., 2016).

The reader may refer to Appendix D.1 for further details on the attacks. Iter-FSGM is essentially equivalent to the Projected Gradient Descent (PGD) with  $\ell_\infty$  projections on the negative loss function (Madry et al., 2018).

We also consider **black-box** version of each of the aforementioned adversarial attacks where the noise is constructed using N-LR. This is to avoid situations where LR might be at an advantage due to the low-rank structure that might enforce a form of gradient masking (Tramèr et al., 2018).

	R18	$\rho$ [DFL]	$\rho$ [ILL]	$\rho$ [IFSGM]
White Box	2-LR	$1.8 \times 10^{-1}$	$9.8 \times 10^{-2}$	$7.6 \times 10^{-2}$
	1-LR	$1.7 \times 10^{-1}$	$1.1 \times 10^{-1}$	$6.0 \times 10^{-2}$
	N-LR	$1.6 \times 10^{-2}$	$2.4 \times 10^{-2}$	$2.1 \times 10^{-2}$
Black Box	2-LR	$5.5 \times 10^{-2}$	$2.0 \times 10^{-1}$	$7.5 \times 10^{-2}$
	1-LR	$4.7 \times 10^{-2}$	$1.8 \times 10^{-1}$	$5.6 \times 10^{-2}$

Table 3: Minimum perturbation required for 99% Adversarial Misclassification by ResNet18 models on CIFAR10. Table 10 in Appendix shows the  $\ell_\infty$  perturbations used.

**Robustness to Adversarial Attacks** In Table 1, we measure the adversarial test accuracy of ResNet18 and ResNet50 models trained on CIFAR10 and CIFAR100 respectively. Adversarial test accuracy measures the accuracy of the model, subjected to an adversarial attack with a fixed perturbation budget, on a test set. The adversary used here is an  $L_\infty$  PGD adversary (or IFSGM) that has two main constraints — the  $\ell_\infty$  radius and the number of attack steps the PGD algorithm can take. The  $\ell_\infty$  radius is chosen from  $\{8/255, 16/255, 32/255, 64/255\}$  with either 7 or 20 attack steps of PGD. This represents a wide variety of severity in the attack model and our LR model performs much better than the N-LR model in all the settings including the black-box settings (refer Table 1). For example, in the case of white-box attack, for C10, R50,  $\ell_\infty = \frac{16}{255}$ , and attack iteration of 20, LR is nearly **10 times more accurate** than N-LR.

Above results clearly indicate that LR provides low-rank representations that are robust to adversarial perturbations and also provide modest improvements on the test accuracy. It is also interesting to note that in terms of model complexity, a more complex model (ResNet50) is significantly more adversarially robust than ResNet18. This was observed in Madry et al. (2018) and the ordering is true for LR models as well. In fact, the difference in adversarial robustness between ResNet18 and ResNet50 is much greater for LR models than for N-LR.

In Table 2, we also compare our LR with other methods that reduce some form of intrinsic dimensions of the parameter space. SNIP (Lee et al., 2019), a pruning technique, increases the sparsity of the parameter, SRN (Sanyal et al., 2020) reduces the (stable) rank and spectral norm of the parameters, and SN (Miyato et al., 2018) reduces the spectral norm of the parameters. We use the best hyper-parameter settings suggested for these approaches in their manuscripts. For a description of these methods and other related approaches please refer to Appendix A. Our method performs much better than all three of these methods indicating that reducing the dimensionality of the representation space is much more effective than doing so for the parameter space when it comes to robustness of the network.

**Accuracy vs the amount of adversarial noise** Next, we compare the change in accuracy of adversarial classification with respect to the actual amount of noise added (as opposed to the perturbation budget as in Table 1). The amount of noise added can be measured using the normalized  $L_2$  dissimilarity measure ( $\rho$ ), defined as:

$$\rho = \mathbb{E} [\|\mathbf{x}_a - \mathbf{x}_d\|_2 / \|\mathbf{x}_d\|_2],$$

where  $\mathbf{x}_d$  and  $\mathbf{x}_a$  are the clean and adversarially perturbed samples, respectively. It measures the magnitude of the noise (Moosavi-Dezfooli et al., 2016) in the input corresponding to a certain adversarial misclassification rate<sup>5</sup>.

Here we also consider another model, for comparison, we call *Bottle-LR* model. It contains an *explicit bottleneck* low-rank layer, rather than LR-layer, which is essentially a fully connected layer without any non-linear activation where the weight matrix  $\mathbf{W} \in \mathbb{R}^{q \times q}$  is parameterized by  $\mathbf{W}_l \in \mathbb{R}^{q \times r}$ , where  $r \leq q$ , so that  $\mathbf{W} = \mathbf{W}_l \mathbf{W}_l^T$ . Note, by design, it can not have rank greater than  $r$ .

Figure 4(a) shows that as the noise increases, the accuracy of N-LR models decreases much faster than the LR models. Specifically, to reach an adversarial mis-classification rate of 50%, our models require

<sup>5</sup>Similar to the setting in Kurakin et al. (2017), the noise is added for a pre-determined number of steps.

about twice the noise as the N-LR or Bottle-LR. *Therefore, for all kinds of attacks we considered, LR models consistently outperform N-LR and Bottle-LR.* More experiments provided in Appendix (Fig 9).

Even though the rank constraint of Bottle-LR is the same as LR models, and they are placed at the same position as the LR layers, the inferior performance of Bottle-RL (sometimes even worst than N-LR) can be explained using the fact that the explicit bottleneck has a *multiplicative* effect on the back-propagated gradients, whereas, LR’s impact on gradients is *additive*. With a bottleneck layer, the gradient of any  $\mathbf{W}_j$  before the bottleneck layer is  $\partial\mathcal{L}/\partial\mathbf{w}_j = (\partial\mathcal{L}/\partial\mathbf{z}_l)\bar{\mathbf{W}}(\partial\mathbf{a}_{l-1}/\partial\mathbf{w}_j)$  where  $\mathbf{a}_l$  and  $\mathbf{z}_l$  are the activations and the pre-activations of the  $l^{th}$  layer respectively. Thus, especially during early stages of training when  $\bar{\mathbf{W}}$  is not yet learned, important directions in  $(\partial\mathbf{a}_{l-1}/\partial\mathbf{w}_j)$  can be cancelled out due to the low-rank nature of  $\bar{\mathbf{W}}$  thus making  $\partial\mathcal{L}/\partial\mathbf{w}_j$  uninformative. In the case of LR, the gradients from  $\mathcal{L}_c$  (depending on  $W$ ) and  $\mathcal{L}$  are additive and thus the low-rank  $\mathbf{W}$  only affects the gradients from  $\mathcal{L}$  additively. The auxiliary loss  $\mathcal{L}_c$  has less direct impact on early training (in terms of classification error). We believe this relative “smoothness” of our approach is the reason why it has a better performance on these other tasks.

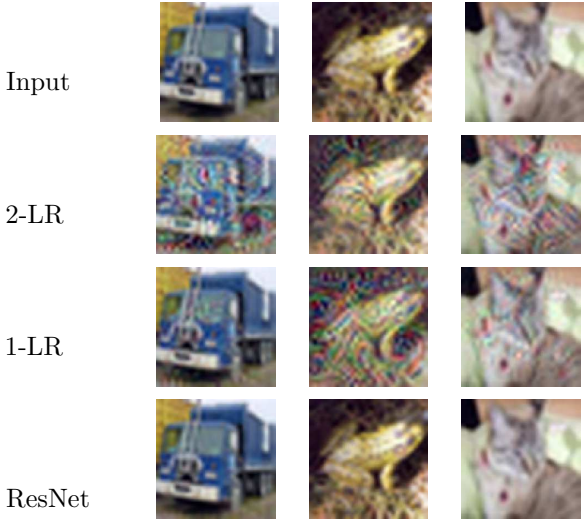


Figure 3: Adversarial images using DeepFool against different classifiers. The images against low-rank (LR) classifiers require more perturbations and are noticeably different.

**Minimum adversarial perturbation for 99% misclassification** Our next experiment is along the lines of that reported in Moosavi-Dezfooli et al. (2016). Table 3 shows the average minimum perturbation (measured by  $\rho$ ) required to make the classifier mis-classify more than 99% of the adversarial examples, constructed from a uniformly sampled subset of the test set. Appendix D.3 describes the setup in greater detail. Even under this scheme of attacks, our models perform better than N-LR as LR models require 4 to 11 times the amount of noise required by N-LR models to be fooled by adversarial attacks. This can be clearly visualized in Figure 3. The adversarial images for 2-LR and 1-LR are noticeably much more perturbed than N-LR.

### 3.2 Noise Stability

To gain some understanding of this visibly better adversarial robustness of LR models, in this section, we study the noise stability behaviour of LR models in detail. Specifically, we show that LR models (and its representations) are significantly more stable to input perturbations at test time even though training was performed using clean data. In addition, we also measure a quantity called *layer cushion* introduced by Arora et al. (2018) that reflects the noise stability properties of layers in deep networks.

**Random Pixel Perturbations** In Table 4, we measure the test accuracy when the input is perturbed with a random additive noise. Specifically, for a given pixel and for a given *pixel perturbation probability*  $p \in \{0.4, 0.6, 0.8, 1.0\}$ , we draw a sample from a Bernoulli distribution parameterized by  $p$  to decide whether to perturb the pixel or not. If the outcome of the draw is 1, the pixel is perturbed with a Gaussian noise drawn from  $\mathcal{N}(0, 128/255)$ . This is done for all pixels in the test set and the test accuracy is measured over this perturbed dataset. For varying levels of perturbation, Table 4 shows that LR models are significantly more stable to Gaussian noise than N-LR. Our experiments indicate that learning a model that cancels out irrelevant directions in the representations suppresses the propagation of the input noise in a way to reduce



Pert. Prob. ( $p$ )		0.4	0.6	0.8	1.0
R50	N-LR	69.7	26.1	12.6	11.3
	1-LR	<b>75.1</b>	<b>34.2</b>	<b>15.8</b>	<b>13.0</b>
R18	N-LR	57.7	27.3	13.0	7.2
	1-LR	<b>75.1</b>	33.0	15.2	11.0
	2-LR	74.1	<b>35.5</b>	<b>16.4</b>	<b>11.5</b>

Table 4: Test accuracy of ResNet50 (R50) and ResNet18(R18) to Gaussian noise  $\mathcal{N}(0, 128/255)$  introduced at each pixel with probability  $p$ . Evaluated on CIFAR10.

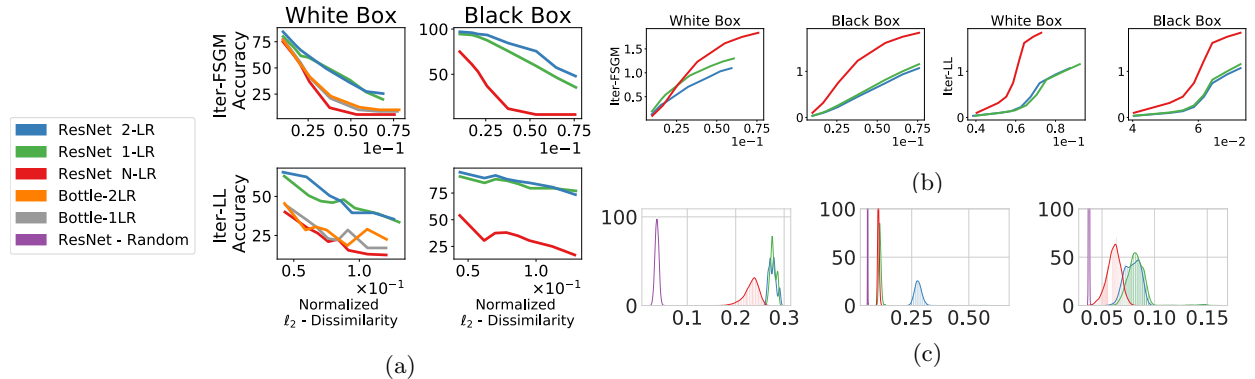


Figure 4: 4(a) shows adversarial accuracy of ResNet18 plotted against magnitude of perturbation (measured by  $\rho$ ) on CIFAR10. 4(b) shows the adversarial Perturbation in Input Space (x-axis) and Perturbation in Representation Space (y-axis) (Lower is better). 4(c) shows the layer cushion for the 1) last FC layer of ResNet18, 2) the last layer in  $3^{rd}$  ResNet block, and 3) the last layer in the  $4^{th}$  ResNet block. (Right is better)

its affect on the output of the model. Interestingly, the level of Gaussian noise seems to not vary the test accuracy as much as the value of  $p$  does.

**Stability of representations** In Figure 4(b), we show how the input adversarial perturbations propagate and impact the feature space representations. Specifically, for a given adversarial perturbation  $\delta$  to an input  $\mathbf{x}$ , the  $x$ -axis is the normalized  $L_2$  dissimilarity score in the input space i.e.  $\|\delta\|^2/\|\mathbf{x}\|^2$  and the  $y$ -axis represents the corresponding quantity in the representation space i.e.  $\|f_\ell^-(\mathbf{x} + \delta) - f_\ell^-(\mathbf{x})\|^2/\|f_\ell^-(\mathbf{x})\|^2$ . The representations  $f_\ell^-(\cdot)$  here are taken from before the last fully connected layer. As our experiments suggest, the LR model significantly attenuates the adversarial perturbations thus making it harder to fool the softmax classifier. This observation further supports the excellent robustness of LR.

**Layer cushion** Arora et al. (2018) gives empirical evidence that deep networks are stable towards injected Gaussian noise and use a variation of this noise stability property to derive more realistic generalization bounds. For any layer  $i$ , Arora et al. (2018) defines the *layer cushion* as the largest number  $\mu_i$  such that for all examples  $\mathbf{x}$  in the training set:  $\mu_i \|\mathbf{W}_i\|_F \|\phi(\mathbf{x}_{i-1})\| \leq \|\mathbf{W}_i \phi(\mathbf{x}_{i-1})\|$  where  $\mathbf{W}_i$  is the weight matrix of the  $i^{th}$  layer,  $\mathbf{x}_{i-1}$  is the pre-activation of the  $i-1$  layer and  $\phi$  is the activation function. Higher the value of  $\mu_i$ , better is the generalization ability of the model. Figure 4(c) shows histogram plots of distribution of this ratio for the examples in CIFAR10 for four models—2-LR, 1-LR, N-LR and a *random network* (randomly initialized, no training done) with the same architecture.

As Figure 4(c) shows, the histograms of the LR models are to the right of the N-LR model, which is further to the right of the randomly initialized network. Interestingly, the layer cushion histograms of the last linear layer as well as the last layer of the 4 residual block is approximately the same for both 1-LR and 2-LR whereas the histogram for the layer cushion of the last layer in the 3rd ResNet block of the 2-LR model is significantly to the right of the 1-LR and N-LR models. This can be explained by the fact that 2-LR is the only model that has the low-rank regularizer after the 3rd ResNet block and it thus has higher layer

<b>R50</b>	Dim	Acc(%)	<b>R18</b>	Dim	Acc(%)
1-LR	2k	<b>78.1</b>	2-LR	16k	<b>91.14</b>
N-LR	2k	75.6	N-LR	16k	90.7
1-LR	10	<b>76.5</b>	2-LR	20	<b>88.5</b>
N-LR	10	68.4	N-LR	20	76.9
1-LR	5	<b>72</b>	2-LR	10	<b>75</b>
N-LR	5	48	N-LR	10	61.7

(a) Representation from before the FC layer, trained on CIFAR-100. Original dimension here is 2k.

(b) Representation from before the last ResNet block, trained on CIFAR10. Original dimension here is 16k.

Table 5: *Dim* represents the size of the *compressed embedding* on which a separate linear classifier was trained.

cushion (*and thus better noise stability*) for the last layer in the 3rd ResNet block. Please refer to Appendix E for more information on these plots and the plots for other layers.

### 3.3 Compression of Model and Embeddings

Experiments in the previous section show that our algorithm induces a low-rank structure in the activation space and that these low-rank activations are significantly more stable to input perturbations. Here we inspect the discriminative power of these embeddings. Further, due to the low dimensionality of the representation space, these learned representations can be compressed without losing their discriminative power. Among other things, we show that low dimensional projections of our embeddings, *with a size of less than 2% of the original embeddings*, can be used for classification with a significantly higher accuracy than similar sized projections of embeddings from a model trained without our training modification (N-LR) on the CIFAR100 dataset.

In order to study compressibility, we use the trained models (N/1/2-LR-ResNet50/18) to construct hybrid max-margin models. Learned representations are first generated using the original trained model on the training set; then a max-margin classifier (such as SVM) is trained on these learned representations. In some of the experiments, before training the max-margin classifier, the learned representations are projected onto a low dimensional space by performing PCA on this set of learned representations. The embedding dimension of the PCA and the particular layer from which the representations are extracted is specified in Table 5. At test time, the original trained model is used to first obtain a representation, if necessary, it is then projected using the learnt PCA projection matrix, and is then classified using the learnt max-margin linear classifier. Further details appear in Appendix C.

**Representation Compression:** Table 5(a) shows that even with sharply decreasing embedding dimension, the hybrid model trained using the LR preserves the accuracy significantly more so than N-LR. *Even with a 5-dimensional embedding (400x compression), the LR model loses only 6% in accuracy, but the N-LR model loses 27%.*

**Model Compression:** A consequence of forcing the activations of the  $\ell^{th}$  layer of the model to lie in a low dimensional subspace with minimal reconstruction error, is that a simpler model can replace the latter parts of the original model without significant reduction in accuracy. Essentially, if we train the hybrid max-margin classifier on the representations obtained from after the third ResNet block, we can replace the entire fourth ResNet block and the last FC layer with a linear classifier. The results of this experiment, in Table 5(b), show evidence of this. *The entire fourth ResNet block along with the last FC layer (containing 8.4M parameters) is replaced by a smaller linear model which has only 0.02 times the number of parameters.* This yields a significant reduction in model size at the cost of a very slight drop in accuracy ( $< 1\%$ ). The second benefit is that as the low dimensional embeddings still retain most of the *discriminative* information, the inputs fed to the linear model have a small number of features.

**Robustness of Max Margin Classifiers:** Finally, we show that the features learned by our models are inherently more linearly discriminative i.e. there exists a linear classifier which can be used to classify these features with a wide margin. To this end, in Table 6, we show that for LR models, the max-margin

	R18	DFL	ILL	IFSGM
White Box	2-LR	<b>0.43</b>	<b>0.55</b>	<b>0.55</b>
	1-LR	0.38	0.35	0.48
	N-LR	0.01	0.04	0.02
Black Box	2-LR	<b>0.44</b>	<b>0.50</b>	<b>0.48</b>
	1-LR	0.29	0.31	0.33

Table 6: Accuracy of classification of adversarial examples by ResNet18 Max Margin Classifiers.

hybrid models are significantly more robust to adversarial attacks than the corresponding original models. Hybrid max-margin models with LR-layers are particularly more robust than hybrid max-margin models without LR-layers against adversarial attacks. Specifically, as seen in Table 6, *a hybrid model with a LR-layer correctly classifies 50% of the examples that had fooled the original classifier while for a similar amount of noise, an N-LR hybrid model has negligible accuracy.* Our experimental setup is explained in Appendix D.5.

## 4 Conclusion

We proposed a low-rank regularizer (LR) that encourages deep neural networks to learn representations that lie in a lower-dimensional linear subspace. We conducted a wide range of experiments to investigate the properties of representations learned by LR and report, among other things, that (i) these representations are robust to both, adversarial and random input perturbations, (ii) LR models significantly attenuate the effects of perturbations introduced in the input space on the representation space (iii) these representations have more discriminatory power than ones trained on representation from models without LR-layers, and (iv) these representations provide extreme compression without compromising much with the accuracy.

It is commonly believed that large sparse feature spaces are better for deep models. What we propose here is the idea that while the features themselves need not be sparse, the existence of a basis in which the feature vectors have a sparse representation can provide benefits. To the best of our knowledge, investigating properties of representations learned from NNs, and the possibility of modifying training procedures to obtain desirable properties in said representations, has remained relatively unexplored. This work shows that these representations possess some intriguing properties, which may well be worthy of further investigation.

## 5 Acknowledgements

AS acknowledges support from The Alan Turing Institute under the Turing Doctoral Studentship grant TU/C/000023. VK is supported in part by the Alan Turing Institute under the EPSRC grant EP/N510129/1. PHS and PD are supported by the ERC grant ERC-2012-AdG 321162-HELIOS, EPSRC grant Seebibyte EP/M013774/1 and EPSRC/MURI grant EP/N019474/1. PHS and PD also acknowledges the Royal Academy of Engineering and FiveAI.

## References

- Arora, S., Ge, R., Neyshabur, B., and Zhang, Y. Stronger generalization bounds for deep nets via a compression approach. In Dy, J. and Krause, A. (eds.), *Proceedings of the 35th International Conference on Machine Learning*, volume 80 of *Proceedings of Machine Learning Research*, pp. 254–263, Stockholmsmässan, Stockholm Sweden, 10–15 Jul 2018. PMLR. URL <http://proceedings.mlr.press/v80/arora18b.html>.
- Denton, E., Zaremba, W., Bruna, J., LeCun, Y., and Fergus, R. Exploiting Linear Structure Within Convolutional Networks for Efficient Evaluation. In *Advances in neural information processing systems*, pp. 1269–1277, apr 2014. URL <http://arxiv.org/abs/1404.0736>.
- Donahue, J., Jia, Y., Vinyals, O., Hoffman, J., Zhang, N., Tzeng, E., and Darrell, T. DeCAF: A Deep Convolutional Activation Feature for Generic Visual Recognition. In *International Conference on Machine Learning*, pp. 647–655, oct 2014. URL <http://arxiv.org/abs/1310.1531>.

- Goodfellow, I. J., Shlens, J., and Szegedy, C. Explaining and Harnessing Adversarial Examples. *arXiv preprint arXiv:1412.6572*, dec 2014. URL <http://arxiv.org/abs/1412.6572>.
- Halko, N., Martinsson, P.-G., and Tropp, J. A. Finding structure with randomness: Probabilistic algorithms for constructing approximate matrix decompositions. *SIAM review*, 53(2):217–288, 2011.
- He, K., Zhang, X., Ren, S., and Sun, J. Deep Residual Learning for Image Recognition. In *2016 IEEE Conference on Computer Vision and Pattern Recognition (CVPR)*, pp. 770–778. IEEE, jun 2016. ISBN 978-1-4673-8851-1. doi: 10.1109/CVPR.2016.90. URL <http://ieeexplore.ieee.org/document/7780459/>.
- Hinton, G. E. and Salakhutdinov, R. R. Reducing the dimensionality of data with neural networks. *Science (New York, N.Y.)*, 313(5786):504–7, jul 2006. ISSN 1095-9203. doi: 10.1126/science.1127647. URL <http://www.ncbi.nlm.nih.gov/pubmed/16873662>.
- Hotelling, H. Canonical correlation analysis (cca). *Journal of Educational Psychology*, pp. 10, 1935.
- Jaderberg, M., Vedaldi, A., and Zisserman, A. Speeding up Convolutional Neural Networks with Low Rank Expansions. In *Proceedings of the British Machine Vision Conference*. BMVA Press, 2014.
- Jain, P., Meka, R., and Dhillon, I. S. Guaranteed rank minimization via singular value projection. In *Advances in Neural Information Processing Systems*, pp. 937–945, 2010.
- Jolliffe, I. *Principal Component Analysis*. Springer-Verlag, 2002. doi: 10.1007/b98835.
- Kumar, S., Mohri, M., and Talwalkar, A. Ensemble nystrom method. In *Advances in Neural Information Processing Systems*, pp. 1060–1068, 2009a.
- Kumar, S., Mohri, M., and Talwalkar, A. Sampling techniques for the nystrom method. In *International Conference on Artificial Intelligence and Statistics*, pp. 304–311, 2009b.
- Kurakin, A., Goodfellow, I., and Bengio, S. Adversarial examples in the physical world. *arXiv preprint arXiv:1607.02533*, 2016.
- Kurakin, A., Goodfellow, I., and Bengio, S. Adversarial machine learning at scale. *International Conference on Learning Representations (ICLR)*, 2017.
- Lee, N., Ajanthan, T., and Torr, P. Snip: Single shot network pruning based on network connectivity. In *International Conference on Learning Representations*, 2019. URL <https://openreview.net/forum?id=B1VZqjAcYX>.
- Madry, A., Makelov, A., Schmidt, L., Tsipras, D., and Vladu, A. Towards deep learning models resistant to adversarial attacks. In *International Conference on Learning Representations*, 2018. URL <https://openreview.net/forum?id=rJzIBfZAb>.
- Meyer, C. D. (ed.). *Matrix Analysis and Applied Linear Algebra*. Society for Industrial and Applied Mathematics, Philadelphia, PA, USA, 2000. ISBN 0-89871-454-0.
- Miyato, T., Kataoka, T., Koyama, M., and Yoshida, Y. Spectral normalization for generative adversarial networks. In *International Conference on Learning Representations*, 2018. URL <https://openreview.net/forum?id=B1QRgziT->.
- Moosavi-Dezfooli, S.-M., Fawzi, A., and Frossard, P. DeepFool: {A} Simple and Accurate Method to Fool Deep Neural Networks. In *CVPR*, pp. 2574–2582. {IEEE} Computer Society, 2016.
- Oyallon, E. Building a regular decision boundary with deep networks. In *Proceedings of the IEEE Conference on Computer Vision and Pattern Recognition*, pp. 5106–5114, 2017.

- Sanyal, A., Torr, P. H., and Dokania, P. K. Stable rank normalization for improved generalization in neural networks and {gan}s. In *International Conference on Learning Representations*, 2020. URL <https://openreview.net/forum?id=H1enKkrFDB>.
- Schmidt, L., Santurkar, S., Tsipras, D., Talwar, K., and Madry, A. Adversarially robust generalization requires more data. In *Advances in Neural Information Processing Systems*, pp. 5014–5026, 2018.
- Sermanet, P., Eigen, D., Zhang, X., Mathieu, M., Fergus, R., and LeCun, Y. OverFeat: Integrated Recognition, Localization and Detection using Convolutional Networks. In *International Conference on Learning Representations (ICLR)*, dec 2014. URL <http://arxiv.org/abs/1312.6229>.
- Szegedy, C., Zaremba, W., Sutskever, I., Bruna, J., Erhan, D., Goodfellow, I., and Fergus, R. Intriguing properties of neural networks. *arXiv preprint arXiv:1312.6199*, 2013.
- Tramèr, F., Kurakin, A., Papernot, N., Goodfellow, I., Boneh, D., and McDaniel, P. Ensemble adversarial training: Attacks and defenses. In *International Conference on Learning Representations*, 2018. URL <https://openreview.net/forum?id=rkZvSe-RZ>.
- Tsipras, D., Santurkar, S., Engstrom, L., Turner, A., and Madry, A. Robustness may be at odds with accuracy. In *International Conference on Learning Representations*, 2019. URL <https://openreview.net/forum?id=SyxAb30cY7>.
- Williams, C. K. I. and Seeger, M. Using the Nyström method to speed up kernel machines. In *Advances in neural information processing systems*, pp. 682–688, 2001.
- Zeiler, M. D. and Fergus, R. Visualizing and Understanding Convolutional Networks. In Fleet, D., Pajdla, T., Schiele, B., and Tuytelaars, T. (eds.), *Computer Vision – ECCV 2014*, pp. 818–833, Cham, 2014. Springer International Publishing. ISBN 978-3-319-10590-1.

# A Alternative Algorithms

## Sparsity and Rank

While various techniques to induce sparsity on weights or activations in neural networks exist, we point out that sparsity doesn't necessarily lead to low rank, e.g., the identity matrix is sparse while being full rank. However, we also look at whether sparsity and rank correlate empirically in the representation space in real trained networks.

Empirically, in ResNet 1-LR, the activations before the 4<sup>th</sup> ResNet block are 39% sparse and the activations after the 4<sup>th</sup> ResNet block are 5% sparse. However, the activations before the 4<sup>th</sup> ResNet block require a larger number of singular values ( $> 1000$ ) to explain greater than 99% of the variance despite the high level of sparsity (39%) whereas the activations after the 4th ResNet block are explained almost totally by about 10 singular values. Thus, sparsity and low rank are not correlated in this case. Technically, being low rank means there exists a basis in which the vector has a sparse representation.

In Table 2, we compare against SNIP (Lee et al., 2019), a popular technique for pruning/increasing sparsity of neural networks. We use a sparsity ratio of 0.7, which was the sparsest network that SNIP could obtain without any drop in test-accuracy. However, it should be noted that adversarial robustness of sparse networks is an active area of research and orthogonal to the ideas proposed in this paper.

## Low Rank Weights

With respect to compression, it is natural to look at low rank approximations of network parameters (Denton et al., 2014; Jaderberg et al., 2014). By factorizing the weight matrix/tensor  $W$ , for input  $x$ , we can get low rank *pre-activations*  $Wx$ . This however does not lead to low rank *activations* as demonstrated both mathematically (by the counter-example below) and empirically.

In Table 2, we compare against SRN (Sanyal et al., 2020) a simple algorithm for reducing the stable rank (a softer version of rank) of linear layers in neural networks. We use the best hyper-parameter obtained from the Sanyal et al. (2020) paper for these experiments.

**Mathematical Counter-Example:** Consider a rank 1 *pre-activation* matrix  $A$  and its corresponding *post-activation*(ReLU) matrix as below. It is easy to see that the rank of *post-activation* has increased to 2.

$$A = \begin{bmatrix} 1 & -1 & 1 \\ -1 & 1 & -1 \end{bmatrix} \quad \text{Relu}(A) = \begin{bmatrix} 1 & 0 & 1 \\ 0 & 1 & 0 \end{bmatrix}$$

**Empirical Result:** In order to see if techniques for low rank approximation of network parameters like Denton et al. (2014) would have produced low rank activations, we conducted an experiment by explicitly making the *pre-activations* low-rank using SVD. Our experiments showed that in spite of setting a rank of 100 to the *pre-activation* matrix, the *post-activation* matrix had full rank. Though all but the first hundred singular values of the *pre-activation* matrix were set to zero, the *post-activation* matrix's 101<sup>st</sup> and 1000<sup>th</sup> singular values were 49 and 7.9 respectively, and its first 100 singular values explained only 94% of the variance.

We try to explain the above empirical results as follows: Theoretically, a bounded activation function lowers the Frobenius norm of the *pre-activation* matrix i.e. the sum of the squared singular values. However, it also causes a smoothing of the singular values by making certain 0 singular values non-zero to compensate for the significant decrease in the larger singular values. This leads to an increase in rank of the *post-activation* matrix.

**Structure in Linear Transformation:** Added to these arguments, it must be noted that widely used transformation in deep networks like convolution layers etc are highly structured and introducing low structure while maintaining the structure is not as simple as doing it for a fully connected layer where the matrix does not have any special structure that needs to be maintained.

## Bottleneck LR Layer

**Bottleneck Layer e.g. Autoencoder:** It is easy to see that the effective dimension of the representation of an input, obtained after passing through a bottleneck layer (like an auto-encoder), will not be greater

than the dimension of the bottleneck layer itself. However, due to the various non-linearities present in the network, while the representation is guaranteed to lie in a low dimensional manifold it is not guaranteed to lie in a low rank (affine) subspace.

**Factorized Linear Layer (LR Bottleneck):** Another alternative is to include the low-rank projection and reconstruction as part of the network instead of as a regularizer so that the LR-layer is an actual layer and not a *virtual* layer. We have indeed experimented with this setup and observed that this often made the training very unstable. Also, if one were to add this bottleneck as a fine-tuning process, the test accuracy of the network decreases by a much higher extent than it does for our method.

## B Algorithmic Details

### B.1 Algorithm for LR Layer

We solve our optimization problem (2) by adding a *virtual* low rank layer that penalizes representations that are far from its closest low rank affine representation. We call it virtual as the layer is not a part of the network’s prediction pathway and can be discarded once the network is trained. Algorithm 2 lists the forward and the backpropagation rules of the LR-layer.

---

#### Algorithm 2 LR Layer

---

- 1: **Input:** Activation Matrix  $A$ , Grad\_input  $g$
  - 2: **Forward Propagation**
  - 3:  $Z \leftarrow W^\top(A + \mathbf{b})$ <sup>6</sup>{Compute the affine *Low rank* projection}
  - 4: **Output :**  $A$ {Output the original activations for the next layer}
  - 5: **Backward Propagation**
  - 6:  $D_1 \leftarrow \frac{\lambda_1}{n} \|Z - (A + \mathbf{b})\|_2^2$  {Computes the reconstruction loss  $\mathcal{L}_c$ }
  - 7:  $D_2 \leftarrow \frac{\lambda_2}{n} \sum_{i=0}^{n-1} |1 - \|\mathbf{a}_i\||$  {Computes the loss for the norm constraint  $\mathcal{L}_N$ }
  - 8:  $D \leftarrow D_1 + D_2$
  - 9:  $g_W \leftarrow \frac{\partial D}{\partial W}, g_i \leftarrow g + \frac{1}{n} \sum_{i=0}^{n-1} \frac{\partial D}{\partial \mathbf{a}_i}$
  - 10: **Output :**  $g_i$  {Outputs the gradient to be passed to the layer before}
  - 11: **Update Step**
  - 12:  $W \leftarrow W - \lambda g_W$  {Updates the weight with the gradient from  $D$ .}
  - 13:  $W \leftarrow \Pi_k^{\text{rank}}(W)$  {Hard thresholds the rank of  $W$ }
- 

The rank projection step in Line 13 in Algorithm 2 is executed by a hard thresholding operator  $\Pi_r^{\text{rank}}(W)$ , which finds the best  $r$ -rank approximation of  $W$ . Essentially,  $\Pi_r^{\text{rank}}(W)$  solves the following optimization problem, which can be solved using a singular value decomposition (SVD). However, the projection can be very expensive due to the large dimension of the representations space (e.g. 16,000). To get around this, we use the ensembled Nystrom SVD algorithm (Williams & Seeger, 2001; Halko et al., 2011; Kumar et al., 2009a).

$$\Pi_r^{\text{rank}}(W) = \underset{\text{rank}(Z)=r}{\text{argmin}} \|W - Z\|_F^2$$

**Handling large activation matrices:** Singular Value Projection (SVP) introduced in Jain et al. (2010) is an algorithm for rank minimization under affine constraints. In each iteration, the algorithm performs gradient descent on the affine constraints alternated with a rank- $k$  projection of the parameters and it provides recovery guarantees under weak isometry conditions. However, the algorithm has a complexity of  $O(mnr)$  where  $m, n$  are the dimensions of the matrix and  $r$  is the desired low rank. Faster methods for SVD for sparse matrices are not applicable as the matrices in our case are not necessarily sparse. We use the ensembled Nystrom method (Williams & Seeger, 2001; Halko et al., 2011; Kumar et al., 2009a) to boost our computational speed at the cost of accuracy of the low rank approximation. It is essentially a sampling based

---

<sup>6</sup> $\mathbf{b} + A$  is computed by adding  $\mathbf{b}$  to every row in  $A$

low rank approximation to a matrix. The algorithm is described in detail in the next section (B.2). Though the overall complexity for projecting  $W$  still remains  $O(m^2r)$ , the complexity of the hard-to-parallelize SVD step is now  $O(r^3)$ , while the rest is due to matrix multiplication, which is fast on modern GPUs.

The theoretical guarantees of the Nyström method hold only when the weight matrix of the LR-layer is symmetric and positive semi-definite (PSD) before each  $\Pi_r^{\text{rank}}(\cdot)$  operation; this restricts the projections allowed in our optimization, but empirically this does not seem to matter. However, note that the PSD constraint is not really a restriction as all projection matrices are PSD by definition. For example, on the subspace spanned by columns of a matrix  $X$ , the projection matrix is  $P = X(X^\top X)^{-1}X^\top$ , which is always PSD. We know that a symmetric diagonally dominant real matrix with non-negative diagonal entries is PSD. With this motivation, the matrix  $W$  is smoothened by repeatedly adding  $0.01\mathbf{I}$  until the SVD algorithm converges where  $\mathbf{I}$  is the identity matrix.<sup>7</sup> This is a heuristic to make the matrix well conditioned (as well as diagonally dominant) and it helps in the convergence of the algorithm empirically.

**Symmetric Low Rank Layer:** The Nyström method requires the matrix  $W$  of the LR-layer to be symmetric and PSD (SPSD), however, gradient updates may make the matrix parameter non-SPSD, even if we start with an SPSD matrix. Reparametrizing the LR-layer fixes this issue; the layer is parameterized using  $W_s$  (to which gradient updates are applied), but the layer projects using  $W = (W_s + W_s^\top)/2$ . After the rank projection is applied to the (smoothened version of)  $W$ ,  $W_s := \Pi_r^{\text{rank}}(W)$  is an SPSD matrix (using Lemma 1 in B.3). As a result the updated  $W$  is also SPSD. This layer also has a bias vector  $\mathbf{b}$  to be able to translate the activation matrix before performing the low rank projection.

## B.2 Ensembled Nyström Method

Let  $W \in \mathbb{R}^{m \times m}$  be a symmetric positive semidefinite matrix (SPSD). We want to generate a matrix  $W_r$  which is a  $r$ -rank approximation of  $W$  without performing SVD on the full matrix  $W$  but only on a principal submatrix<sup>8</sup>  $Z \in \mathbb{R}^{l \times l}$  of  $W$ , where  $l \ll m$ . We sample  $l$  indices from the set  $\{1 \dots m\}$  and select the corresponding columns from  $W$  to form a matrix  $C \in \mathbb{R}^{m \times l}$ . In a similar way, selecting the  $l$  rows from  $C$  we get  $Z \in \mathbb{R}^{l \times l}$ . We can rearrange the columns of  $W$  so that

$$W = \begin{bmatrix} Z & W_{21}^T \\ W_{21} & W_{22} \end{bmatrix} \quad C = \begin{bmatrix} Z \\ W_{21} \end{bmatrix}$$

According to the Nyström approximation, the low rank approximation of  $W$  can be written as

$$W_r = CZ_r^+C^T \quad (3)$$

where  $Z_r^+$  is the pseudo-inverse of the best  $r$  rank approximation of  $Z$ . Hence, the entire algorithm is as follows.

- Compute  $C$  and  $Z$  as stated above.
- Compute the top  $r$  singular vectors and values of  $Z : U_r, \Sigma_r, V_r$ .
- Invert each element of  $\Sigma_r$  as this is used to get the Moore pseudo-inverse of  $Z_r$ .
- Compute  $Z_r^+ = U_r \Sigma_r^{-1} V_r$  and  $W_r = CZ_r^+C^T$ .

Though by trivial computation, the complexity of the algorithm seems to be  $O(l^2r + ml^2 + m^2l) = O(m^2r)$  (In our experiments  $l = 2r$ ), it must be noted that the complexity of the SVD step is only  $O(k^3)$  which is much lesser than  $O(m^2r)$  and while matrix multiplication is easily parallelizable, parallelization of SVD is highly non-trivial and inefficient.

To improve the accuracy of the approximation, we use the ensembled Nyström sampling based methods (Kumar et al., 2009a) by averaging the outputs of  $t$  runs of the Nyström method. The  $l$  indices for

<sup>7</sup>The computation of the singular value decomposition sometimes fail to converge if the matrix is ill-conditioned

<sup>8</sup>A principal submatrix of a matrix  $W$  is a square matrix formed by removing some columns and the corresponding rows from  $W$  (Meyer, 2000)



selecting columns and rows are sampled from an uniform distribution and it has been shown (Kumar et al., 2009b) that uniform sampling performs better than most sampling methods. **Theorem 3** in Kumar et al. (2009a) provides a probabilistic bound on the Frobenius norm of the difference between the exact best  $r$ -rank approximation and the Nyström sampled  $r$ -rank approximation.

### B.3 Lemma 1

**Lemma 1.** *If  $X \in \mathbb{R}^{m \times m}$  is a SPSD matrix and  $X_r \in \mathbb{R}^{m \times m}$  is the best Nyström ensemble, column sampled  $r$ -rank approximation of  $X$ , then  $X_r$  is SPSD as well. (Proof in Appendix B.3)*

*Proof.* By the Construction of the Nyström SVD algorithm, we know that  $X_r = CW_r^+ C^T$ . We will first show that  $W_r^+$  is a symmetric matrix.

We know that  $X$  is SPSD. Let  $I$  be a sorted list of distinct indices such that  $|I| = l$ . Then by construction of  $W$ ,

$$W_{i,j} = X_{I[i],I[j]}$$

Hence, as  $X_{I[i],I[j]} = X_{I[j],I[i]}$ ,  $W$  is symmetric.

At this step, our algorithm adds  $\delta \cdot I$  to  $W$  where  $\delta \geq 0$ . It is easy to observe that  $W + \delta \cdot \mathcal{I}$  is positive semidefinite.

Consider a vector  $a \in \mathbb{R}^{|X|}$ . Create a vector  $\bar{a} \in \mathbb{R}^m$  where

$$\bar{a}_i = \begin{cases} 0 & \text{if } i \notin I \\ a_i & \text{o.w.} \end{cases}$$

$$a^\top (W + \delta \cdot \mathcal{I}) a = \bar{a}^\top X \bar{a} + \delta \cdot a^\top \mathcal{I} a \geq 0 + \delta \|a\|^2 \geq 0 \quad (4)$$

Let  $W + \delta \mathcal{I}$  be the new  $W$  and (4) shows that  $W$  is positive semidefinite.

Now we will show that  $X_r$  is symmetric as well. As  $W$  is symmetric, there exists an orthogonal matrix  $Q$  and a non-negative diagonal matrix  $\Lambda$  such that

$$W = Q\Lambda Q^T$$

We know that  $W_r = Q_{[1:r]}\Lambda_{[1:r]}Q_{[1:r]}^T$  and  $W_r^+ = Q_{[1:r]}\Lambda_{[1:r]}^{-1}Q_{[1:r]}^T$ . Hence,

$$\begin{aligned} X_r &= CW_r^+ C^T \\ &= CQ_{[1:r]}\Lambda_{[1:r]}^{-1}Q_{[1:r]}^T C^T \\ X_r^T &= (CQ_{[1:r]}\Lambda_{[1:r]}^{-1}Q_{[1:r]}^T C^T)^T \\ &= CQ_{[1:r]}\Lambda_{[1:r]}^{-1}Q_{[1:r]}^T C^T \\ &= X_r \end{aligned}$$

$\therefore X_r$  is symmetric. We can also see that the  $X_r^T$  is positive semi definite by pre-multiplying and post multiplying it with a non-zero vector and using the fact that  $W_r^+$  is positive semi-definite.  $\square$

## C Experimental details with additional experiments

In this section, we first describe the training setting and then describe the setting of each experiment in greater detail so that they can be easily reproduced.

**Experimental Settings:** We used a single NVIDIA RTX6000 for training our networks. All our experiments were run with a learning rate of 0.1 for 350 epochs with a batch size of 128 with the learning reduced reduced to 0.01 and 0.001 on the 150th and 250th epoch respectively. The hyper-parameter  $l$  in the

Models		Acc (%)	Acc(%)			
Models	Acc (%)	R18 2-LR	97.86	Models	Coarse	Fine
VGG19 2-LR	<b>89.8</b>	R18 1-LR	<b>97.98</b>	R50 1-LR	<b>78.1</b>	48
VGG19 N-LR	89.1	R18 N-LR	97.97	R50 N-LR	75.6	<b>52</b>
(a) CIFAR10		R18 Bottle-2LR	97.70	R50 Bottle-1LR	76	38
		VGG19 2-LR	<b>97.79</b>	(c) CIFAR-100		
		VGG19 N-LR	97.21			
		(b) SVHN				

Table 7: Table 7(a) shows test accuracy on CIFAR10 for VGG19, Table 7(b) shows test accuracy on SVHN for ResNet18 and VGG19, and Table 7(c) shows the transfer learning experiment as described below.

Nyström method was set to double of the target rank. The model was pre-trained with SGD for the first 50 epochs and then Algorithm 2 was applied. The rank cutting operation was performed every 10 iterations.

The target rank for the LR-layers, which were placed before the FC layers was set to 100 while the target rank for the LR-layer before the last ResNet block was set to 500. However, experiments suggest that this hyper-parameter is **not very crucial** to the training process as the training procedure converged the effective rank of the *activation matrix* to a value lesser than the designated target ranks.

In this section, we also show experiments using VGG19 2-LR. It contains two LR-layers. The VGG model has three FCs after 16 convolution layers. The LR-layers are before the 1st and 3rd FC layers (to maximize the distance between them).

We also report results on the fine labels of CIFAR100 and on SVHN in this section. For the SVHN dataset, as is common practice, we used both the training dataset as well as the extra examples without any data augmentation.

The linear classifier in the *hybrid max-margin* model is trained using SGD with hinge loss and  $L_2$  regularization with a coefficient of 0.01. The learning rate is decreased per iteration as  $\eta_t = \frac{\eta_0}{(1+\alpha t)}$  where  $\eta_0$  and  $\alpha$  are set by certain heuristics<sup>9</sup>.

### C.1 Experiments on test accuracy

We investigate whether the additional constraints on training have any significant effect on model performance. Tables 1,7(a), and 7(b) show that the additional constraints cause no loss in accuracy. In some cases, we even *observe modest gains in performance*.

To test whether the learned representations can be used in a different task, we conduct a transfer learning exercise where embeddings generated from a ResNet-50 model, trained on the coarse labels of CIFAR-100, are used to predict the fine labels of CIFAR-100. A set of ResNet-50 hybrid max-margin classifiers are trained for this purpose on these embeddings. First, two ResNet-50 models were trained with and without the LR-layer respectively on the coarse labels of CIFAR-100. Then, 2048 dimensional embeddings were extracted from after the fourth ResNet block using the train set and the test set of CIFAR 100 for both the models. Essentially, this resulted in two new datasets for training the linear classifiers - one for the LR model and the other for the N-LR model.

The embeddings from each train set were used to train a separate max-margin linear classifier with the same hyper-parameters as described above but by replacing the coarse labels with fine labels. The accuracy of the linear classifier trained on the representations from the LR model and the N-LR model are reported in the third column of Table 7(c). The results of the same experiment, when the linear model was trained on the coarse labels are reported in the second column of Table 7(c). It is surprising that the low rank model performs well at all in this experiment as one would expect that all information in the representations that are not strictly required in the classification of original task are discarded from the model.

<sup>9</sup><https://goo.gl/V995mD>

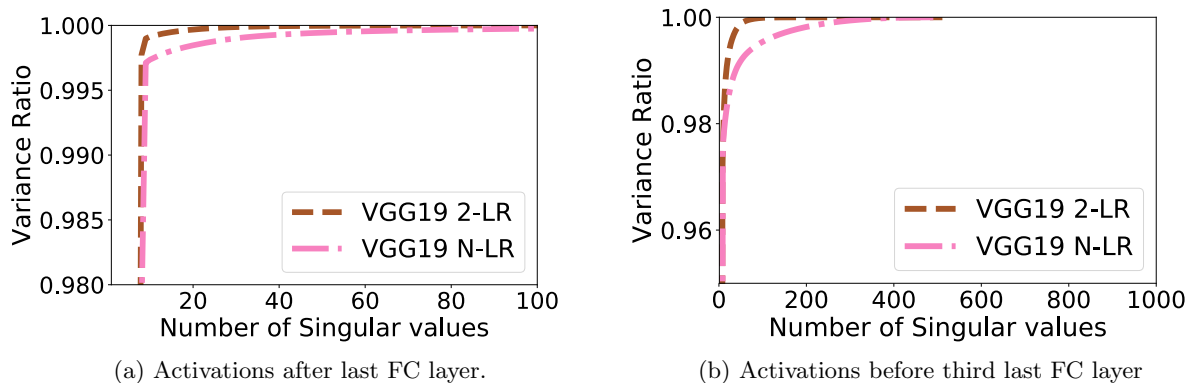


Figure 5: Variance Ratio captured by varying number of Singular Values in VGG19 trained on CIFAR10.

Table 7(c) shows that the LR model suffers a small loss of 4% in accuracy as compared to the N-LR model when its embeddings are used to train a max-margin classifier for predicting fine labels. It should be noted that the accuracy of the LR model actually increases when the max-margin classifier is trained to perform the original task, i.e. classifying the coarse labels. On the other hand, the Bottle-LR model suffers a loss of 14% in accuracy compared to N-LR model and shows no significant advantage in the original task either.

#### Effective rank of activations for VGG and SVHN :

In Figure 5, we plot the variance ratio of representations obtained before the first and third FC layers of VGG19 models trained on CIFAR10. The LR models show a better low rank structure than N-LR models and is consistent with experiments on ResNet18.

In Figure 6, we plot the variance ratio of representations obtained before and after the last resnet block of a ResNet18 models trained on SVHN. The LR models show a better low rank structure than N-LR models and is consistent with experiments on CIFAR10.

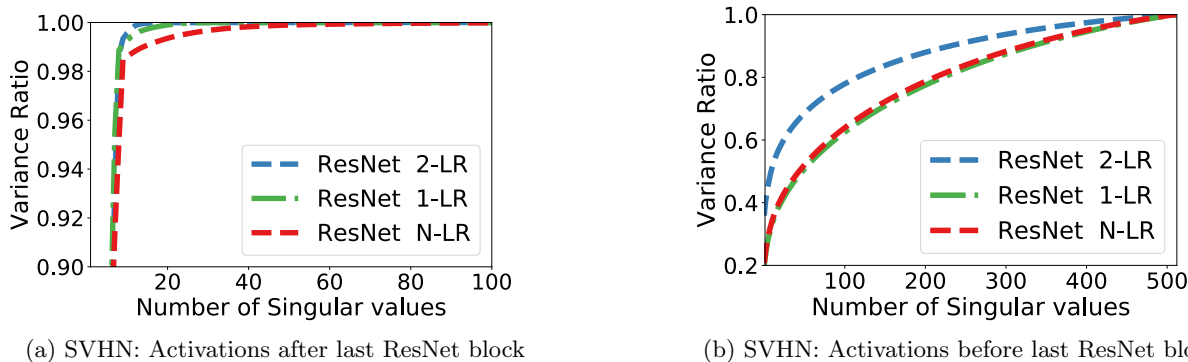
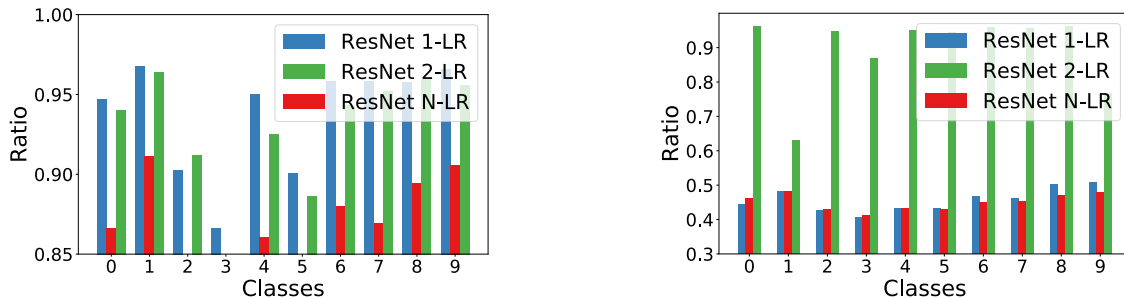


Figure 6: Variance Ratio captured by varying number of Singular Values in ResNet18 trained on SVHN.

## C.2 Additional Classification Experiments for low dimensional embeddings

In the first experiment, reported in Table 5(a), we trained two ResNet-50 hybrid max-margin models -with and without the LR-layer respectively- on the 20 super-classes of CIFAR-100. As our objective here is to see if the embeddings and their low dimensional projections could be effectively used for discriminative tasks, we used PCA, with standard pre-processing of scaling the input, to project the embeddings onto a low dimensional space and then trained a linear maximum margin classifier on it.

The experiments in Table 5(b) were run with ResNet-18 on CIFAR-10. Two ResNet-18 max-margin



(a) 512 dimensional activations from after last ResNet block.

(b) 16k dimensional activations from before last ResNet block.

Figure 7: Class wise variance ratio of one singular values for the activations before the last ResNet block.

classifiers - with and without the LR-layer respectively- were trained on CIFAR-10. The representations were obtained from before the fourth ResNet block and had a dimension of 16,384. Similar to the previous experiment, we used PCA, with standard pre-processing, to obtain low dimensional projections and then trained a linear max margin classifiers on it. The test set of CIFAR10 was converted using the same ResNet models and projected using the same PCA vectors and then the accuracy of the linear classifier on it is reported in Table 5(b) for varying target dimensions of PCA projections.

<b>V19</b>	Dim	Acc(%)
2LR	512	<b>89.8</b>
NLR	512	89.7
2LR	20	<b>89.85</b>
NLR	20	89.78
2LR	10	<b>89.79</b>
NLR	10	89.65

Table 8: Representation from before the third last FC layer of a VGG19 trained on CIFAR-10.

Similar experiments were conducted with VGG19 on CIFAR10 and the results are reported in Table 8. As expected, due to the smaller size of the representation space, the difference in accuracy here is less stark than the case of ResNet. This is because of two reasons - 1. The dimension of the activation layer in ResNet before the last ResNet block is 16,384 whereas the activations before the third last FC layer is only 512. 2. Figure 5 shows that the difference in the variance ratio between the LR and the N-LR network is much smaller as compared to Figure 2 for ResNets.

### C.3 Class wise variance

In this experiment, we plot the variance ratio captured by the first singular value (i.e. the inverse stable rank) for embeddings of examples restricted to individual classes. Figure 7(a) shows the variance ratio captured by the largest singular value for the activations before the last FC layer while Figure 7(b) shows the variance ratio captured by the largest singular value for the activations before the last ResNet block. These experiments give us some idea about the extent to which the set of basis vectors assigned to individual classes are intersecting. Figure 2(a) shows that the rank of the entire activation matrix is almost 10. Figure 7(a) shows that the first singular vector captures a huge portion of the variance of the restriction of the activation matrix on each individual classes. It, thus, gives us an intuition that, by sub-additivity of rank, the sets of basis vectors explaining the activations belonging to each individual classes are less intersecting than it is in the case of the model trained without the LR-layer.

## C.4 Clusters of low dimensional embeddings

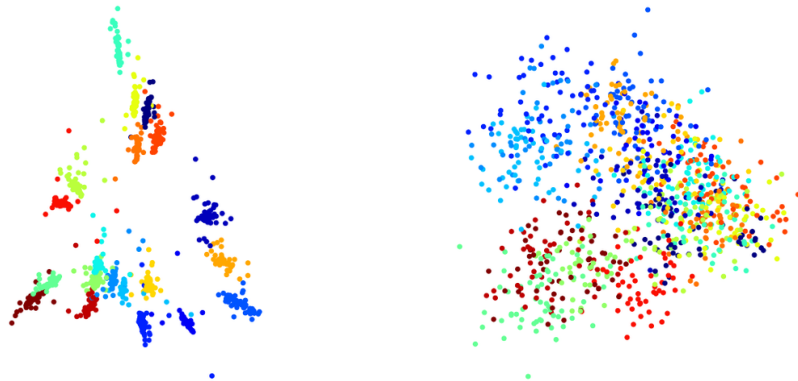


Figure 8: 2-D PCA projection of representations from ResNet50 trained on coarse labels of CIFAR 100 with (left) and without (right) low-rank constraints, colored according to the original 20 coarse labels.

Figure 8 shows the two dimensional projections of the 2048 dimensional embeddings obtained from ResNet-50-LR and ResNet-50-N-LR. The coloring is done according to the coarse labels of the input. We can see that the clusters are more separable in the case of the model with LR-layer than the model without, which gives some insight into why a max-margin classifier performs better for the LR model than the N-LR model. Thus, the representations of the low rank model are more discriminative in the sense that for the low rank representations there are low dimensional linear classifiers that can classify the dataset with a higher margin than the vanilla models.

## D Adversarial Attacks

### D.1 Types of Attacks

Here,  $\mathbf{x}_d$  refers to an example from the data distribution and  $\mathbf{x}_a$  the adversarially perturbed version of  $\mathbf{x}_d$ . For vectors  $\mathbf{z}$  and  $\mathbf{x}$ , let  $\text{clip}_{\mathbf{x},\epsilon}(\mathbf{z})$  denote the element-wise clipping of  $\mathbf{z}$ , with  $z_i$  clipped to the range  $[x_i - \epsilon, x_i + \epsilon]$ .

- Iter-FSGM- The Fast Sign Gradient Method (FSGM) Goodfellow et al. (2014) was proposed as the existing methods (Szegedy et al. (2013)) of the time were slow. FSGM tries to maximize the loss function by perturbing the input slightly. Iterative Fast Sign Gradient method (Iter-FSGM) is a simple extension of FSGM that follows the following simple iterative step.

$$\begin{aligned} \mathbf{x}_a^0 &= \mathbf{x}_d, \\ \mathbf{x}_a^{n+1} &= \text{clip}_{\mathbf{x},\epsilon}(\mathbf{x}_a^n + \alpha \cdot \text{sign}(\nabla_{\mathbf{x}_a^n} \mathcal{L}(\mathbf{x}_a^n, \mathbf{y}_t))) \end{aligned} \tag{5}$$

- Iter-LL-FSGM- Iter-FSGM is an untargeted attack. Iterative less likely fast sign gradient method (Iter-LL-FSGM) (Kurakin et al., 2017) is a way to choose the target label wisely. Consider  $\mathbb{P}_M(\mathbf{y}|\mathbf{x})$  to be the probability assigned to the label  $\mathbf{y}$ , for the example  $\mathbf{x}$ , by the model  $M$ . In this attack, the target is set as  $\mathbf{y}_t^n = \text{argmin}_{\mathbf{y} \in \mathcal{Y}} \mathbb{P}_M(\mathbf{y}|\mathbf{x}^n)$  and the following iterative update steps are performed.

$$\begin{aligned} \mathbf{x}_a^0 &= \mathbf{x}_d, \\ \mathbf{x}_a^{n+1} &= \text{clip}_{\mathbf{x},\epsilon}(\mathbf{x}_a^n - \alpha \cdot \text{sign}(\nabla_{\mathbf{x}_a^n} \mathcal{L}(\mathbf{x}_a^n, \mathbf{y}_t^n))) \end{aligned} \tag{6}$$

Intuitively, this method picks the least likely class in each iteration and then tries to increase the probability of predicting that class. In both of these methods,  $\alpha$  was set to 1 as was done in Kurakin et al. (2017).

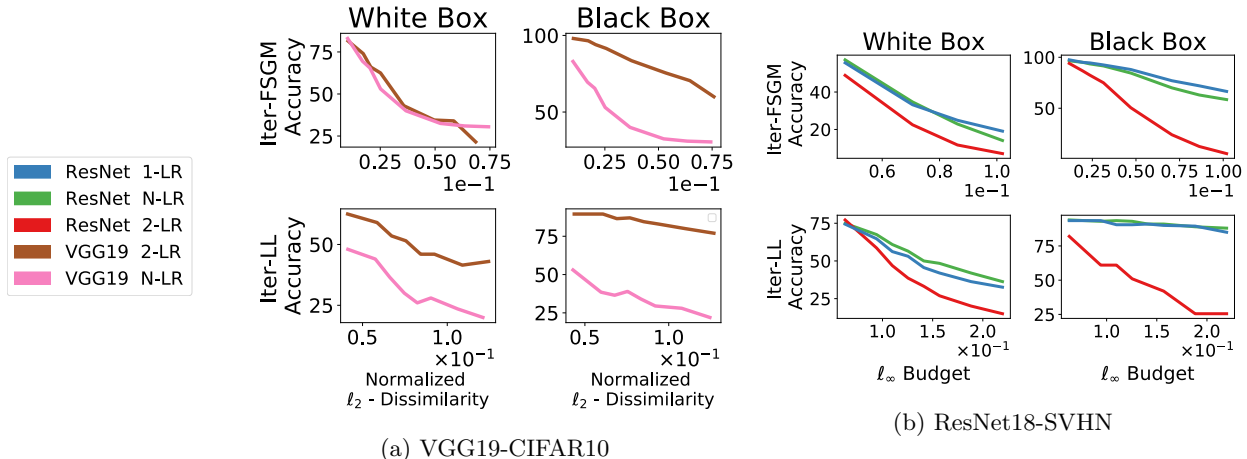


Figure 9: Adversarial accuracy plotted against magnitude of perturbation.

- DeepFool- Moosavi-Dezfooli et al. (2016) describes the DeepFool procedure to find the optimal (smallest) perturbation for the input  $\mathbf{x}$  that can fool the classifier. In the case of affine classifiers, DeepFool finds the closest hyper-plane of the boundary of the region where the classifier returns the same label as  $\mathbf{x}$  and then adds a small perturbation to cross the hyper-plane in that direction.

As deep net classifiers are not affine, the partitions of the input space where the classifier outputs the same label are not polyhedrons. Hence, the algorithm takes an iterative approach. Specifically, the algorithm assumes a linearization of the classifier around  $\mathbf{x}$  to approximate the polyhedron and then it takes a step towards the closest boundary. For a more detailed explanation please look at Moosavi-Dezfooli et al. (2016).

## D.2 Further Experiments on Adversarial Robustness

In Table 9, we show the adversarial test accuracy for varying perturbation budgets for ResNet50 trained on the fine labels of CIFAR100. Low Rank models, not have the best adversarial test accuracies but also the best natural test accuracies.

		Adversarial Test Accuracy(%)								Clean Test Accuracy (%)	
		8/255		10/255		16/255		20/255			
$L_\infty$ radius	Attack iterations	7	20	7	20	7	20	7	20		
White Box	R50	N-LR	27.8	21.8	25.2	17.7	21.1	17.7	19.4	7.6	77.2
		1-LR	<b>28.8</b>	<b>23.6</b>	<b>26.8</b>	<b>21.4</b>	<b>24.4</b>	<b>17.8</b>	<b>23.5</b>	<b>16.5</b>	<b>77.7</b>
Black Box	R50	1-LR	38.3	32.8	34.3	26.4	28.9	15.0	27.0	11.7	-

Table 9: Adversarial Test Accuracy against a  $\ell_\infty$  constrained PGD adversary with the  $\ell_\infty$  radius bounded by  $\epsilon$  and the number of attack steps bounded by  $\tau$ . R50 and R18 denotes ResNet50 and ResNet18 respectively. C10 and C100 refer to CIFAR10 and CIFAR100 (Coarse labels) respectively.

In Figure 9, we compare the change in the adversarial test accuracy with respect to the amount of adversarial noise added for ResNet18 models trained on SVHN 9(b) and VGG19 on CIFAR10 9(a).

## D.3 Minimum Perturbation for a successful Attack

Table 3 lists the minimum perturbation required to fool the classifier under the particular attack scheme. For Iter-FSGM and Iter-LL-FSGM, there are essentially three hyper-parameters( $t, \alpha, \epsilon$ ) in the experiments as can be seen below.

Iter-FSGM

$$\begin{aligned}
 & \text{Repeat } t \text{ times} & (7) \\
 & \mathbf{x}_a^0 = \mathbf{x}_d, \\
 & \mathbf{x}_a^{n+1} = \text{clip}_{\mathbf{x}, \epsilon}(\mathbf{x}_a^n + \alpha \cdot \text{sign}(\nabla_{\mathbf{x}_a^n} \mathcal{L}(\mathbf{x}_a^n, \mathbf{y}_t)))
 \end{aligned}$$

Iter-LL-FSGM

$$\begin{aligned}
 & \text{Repeat } t \text{ times} & (8) \\
 & \mathbf{x}_a^0 = \mathbf{x}_d, \\
 & \mathbf{x}_a^{n+1} = \text{clip}_{\mathbf{x}, \epsilon}(\mathbf{x}_a^n - \alpha \cdot \text{sign}(\nabla_{\mathbf{x}_a^n} \mathcal{L}(\mathbf{x}_a^n, \mathbf{y}_t)))
 \end{aligned}$$

Following the convention of Kurakin et al. (2017), we set  $\alpha = 1$ . We tuned the hyper-parameter  $\epsilon$  function to obtain the smallest  $\epsilon$  that resulted in over 99% misclassification accuracy for some  $t$  and then repeated the experiments until such a  $t$  was achieved. Finally  $\rho$  was calculated.

Algorithm 2 in Moosavi-Dezfooli et al. (2016) gives details about the DeepFool algorithm for multi-class classifiers. The algorithm returns the minimum perturbation  $r(\mathbf{x})$  to make the classifier misclassify the instance  $\mathbf{x}$ . The  $L_2$  dissimilarity is obtained by calculating  $\rho = \frac{r(\mathbf{x})}{\|\mathbf{x}\|_2}$

For the benefit of reproducibility of experiments, we list the values of  $\epsilon$  for Iter-LL-FSGM and Iter-FSGM in Table 10 corresponding to the values in Table 3 . The values of the perturbation budget also show that the minimum perturbation required for 99% mis-classification is much higher for LR models than N-LR models. For DeepFool, we used the publicly available code <sup>10</sup>.

	Model	$\epsilon$ [Iter-LL-FSGM ]	$\epsilon$ [Iter-FSGM ]
White Box	ResNet <b>2-LR</b>	0.04	0.02
	ResNet <b>1-LR</b>	0.06	0.01
	ResNet <b>N-LR</b>	0.01	0.01
Black Box	ResNet <b>1-LR</b>	0.08	0.01
	ResNet <b>2-LR</b>	0.1	0.01

Table 10: Value for  $\epsilon$  required for Adversarial Misclassification corresponding to Table 3.



Figure 10: For each model, original images are on the top row and the images generated by DeepFool are below.

<sup>10</sup><https://github.com/LTS4/DeepFool/blob/master/Python/deepfool.py>

We also look at some of the adversarial images generated by DeepFool in Figure 10. We observe that it is immediately clear that the adversarial images are different from the original images in the case of LR models whereas it is not so apparent in the case of N-LR models.

#### D.4 Unstability of Adversarial Attacks

An interesting observation is that the values of  $\rho$  in Table 3 are lower than those in Figure 4(a) though the attacks have a higher rate of success. To explain this behaviour, we show empirical evidence that an attack that adds noise for a fixed number of steps (Kurakin et al., 2017, 2016) to the input is significantly weaker than one that stops on successful misclassification. The essential difference between the attacks in Figure 4(a) and Table 3 is in the number of iterations for which the updates (Step 7 and Step 8) are executed. In Figure 4(a), the step is executed  $t$  times whereas in Table 3, the updates are executed until the classifier makes a mistake. It would be natural to expect that once a classifier has misclassified an example, adding



Figure 11: This shows that an adversarial example that has successfully fooled the classifier in a previous step can be classified correctly upon adding more perturbation. Figure 11(a) and 11(b) refers to the two attack schemes - Iter-LL-FSGM and Iter-FSGM respectively.

more adversarial perturbation will not make the classifier classify it correctly. However, Figure 11 suggests that a misclassified example can be possibly classified correctly upon further addition of noise.

Let  $y_a(\mathbf{x}; k)$  be the label given to  $\mathbf{x}$  after adding adversarial perturbation to  $\mathbf{x}$  for  $k$  steps. We define *instantaneous accuracy* ( $a_{\mathcal{I}}(k)$ ) and *cumulative accuracy* ( $a_{\mathcal{C}}(k)$ ) as

$$a_{\mathcal{I}}(k) = 1 - \frac{1}{m} \sum_{i=1}^m \mathcal{I}_{0,1} \{y_a(\mathbf{x}; k) \neq y_a(\mathbf{x}; 0)\}; \quad a_{\mathcal{C}}(k) = 1 - \frac{1}{m} \sum_{i=1}^m \max_{1 \leq j \leq k} \{\mathcal{I}_{0,1} \{y_a(\mathbf{x}; j) \neq y_a(\mathbf{x}; 0)\}\}$$

In Figure 11, we see the *instantaneous accuracy* and the *cumulative accuracy* for ResNet 1-LR where  $\alpha = 0.01, \epsilon = 0.1$  and  $t$  is plotted in the x-axis. The cumulative accuracy is by definition a non-increasing sequence. However, surprisingly the instantaneous accuracy is not monotonic and has a lower rate of decrease than the cumulative accuracy. It also appears to stabilize at a value much higher than the cumulative accuracy.

#### D.5 Adversarial Attack on Maximum Margin Model

Here, we train max-margin classifiers on representations of images obtained from different ResNet models (similar to Section C.2) and see whether the representations of adversarial images, that had successfully fooled the ResNet model, can fool the max-margin classifier as well. We train a variety of hybrid max-margin models with ResNet18-1-LR, ResNet18-2-LR, and ResNet18-N-LR along with black box versions of the same. Then we generate adversarial examples for all three attacks (both black box and white box) on the trained ResNet models (not the hybrid models). Then we use these adversarial examples to attack the corresponding max-margin models and report the accuracy of the max-margin models in Table 6.



To perform a fair comparison with the hybrid ResNet18-N-LR, it is essential to add a similar amount of noise to generate the examples for the hybrid ResNet18-N-LR as is added to hybrid ResNet18-1-LR. The adversarial examples are hence generated by obtaining the gradient using ResNet18-N-LR but stopping the iteration only when the adversarial example could fool ResNet18-1-LR. This is, in-fact, the black box attack on ResNet18-1-LR. As Table 6 suggests, the max-margin classifiers are not only more robust to adversarial examples in general but are especially more robust when the representations come from LR models than N-LR models.

## E Noise Cancellation Properties

Here we plot a quantity called *layer cushion*, first mentioned in Arora et al. (2018), for various layers in ResNet18 1-LR, ResNet18 2-LR, ResNet18 N-LR and a randomly initialized ResNet. As suggested in Arora et al. (2018), this quantity appears in the denominator in the generalization bound of the network and has a positive correlation with the noise-cancellation property of the network. Thus a higher value of this quantity can be used to justify the low sensitivity of the network to noise.

The motivation for these quantity is that if the “real” data  $\mathbf{x}$  is more aligned with the high singular values of the linear transformations, the linear transformations are more robust to noise at that point  $\mathbf{x}$ . It can roughly be thought of as the inverse of the sensitivity of the transformation. It measures the ratio of the norm of the actual output of the layer at  $\mathbf{x}$  with the upper bound on the norm of the output at  $\mathbf{x}$ . If this quantity is large for most  $\mathbf{x}$ , it means that most of the signal is aligned with the high singular values of the linear transformation, which means that the transformation is more resilient to noise. This partly explains why the network attenuates the adversarial noise at the data points. For any layer  $i$ , the layer cushion is defined as the largest number  $\mu_i$  such that the following holds for all examples  $\mathbf{x} \in \mathcal{S}$  where  $\mathcal{S}$  is the training set.

$$\mu_i \|\mathbf{W}_i\|_F \|\phi(\mathbf{x}_{i-1})\| \leq \|\mathbf{W}_i \phi(\mathbf{x}_{i-1})\|$$

$\mathbf{W}_i$  is the weight matrix of the  $i^{\text{th}}$  layer,  $\mathbf{x}_i$  is the pre-activation of the layer and  $\phi$  is the activation function. As observed by Arora et al. (2018), higher the value of  $\mu_i$ , better is the generalization ability of the model. Here we plot a distribution of the ratio for the examples in the dataset.

### E.1 Layer Cushion for ResNet18 on CIFAR10

The following corresponds to the four ResNet blocks in ResNet18. Each block has two smaller sub-blocks where each sub-block has two convolutional layers. The value of layer cushion for these modules of each of these blocks are plotted below. Note that only 2-LR shows an increased cushion in Layer 3 whereas both 1-LR and 2-LR have higher cushions in all other layers.

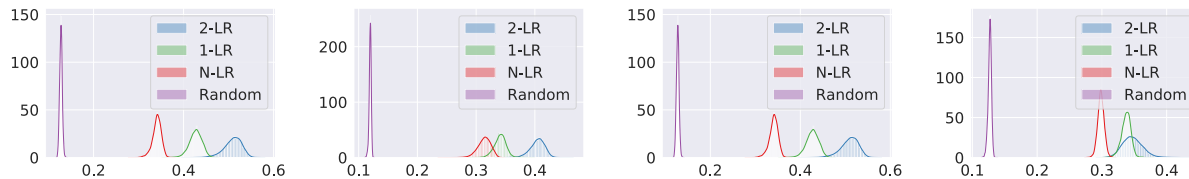


Figure 12: Cushion of Layer 1

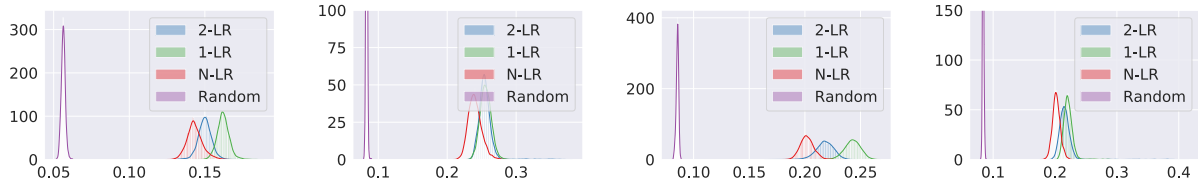


Figure 13: Cushion of Layer 2

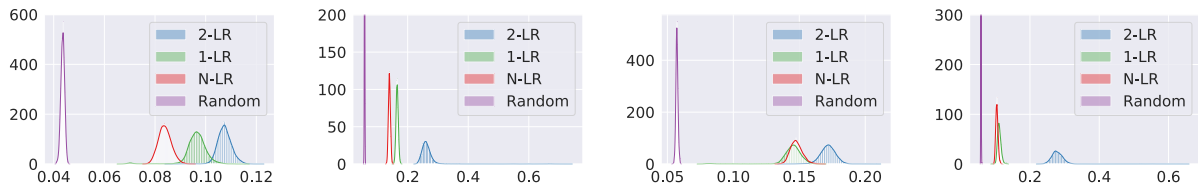


Figure 14: Cushion of Layer 3

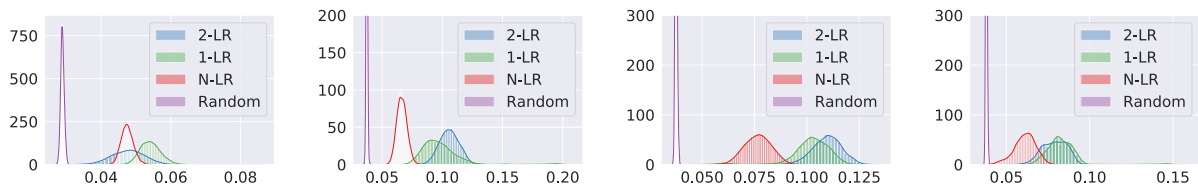


Figure 15: Cushion of Layer 4

## E.2 ResNet18 on SVHN

**Adversarial Noise Attenuation for SVHN** In Figure 16, we plot experiments similar to the one in 4(b) for SVHN dataset and we observe a similar trend.

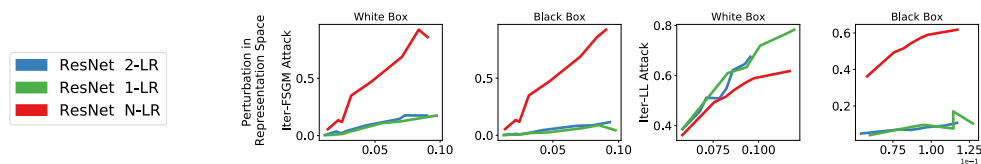


Figure 16: Adversarial Perturbation in Input Space and Perturbation in Representation Space in SVHN

**Layer Cushion for SVHN** The following correspond to ResNet blocks. Each block has two smaller sub-blocks where each sub-block has two convolutional layers. The value of layer cushion for these modules of one block are plotted below.

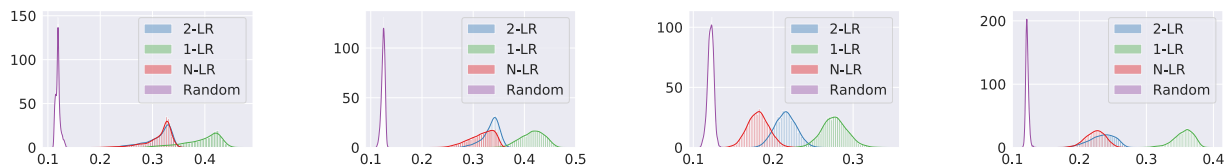


Figure 17: Cushion of Layer 1

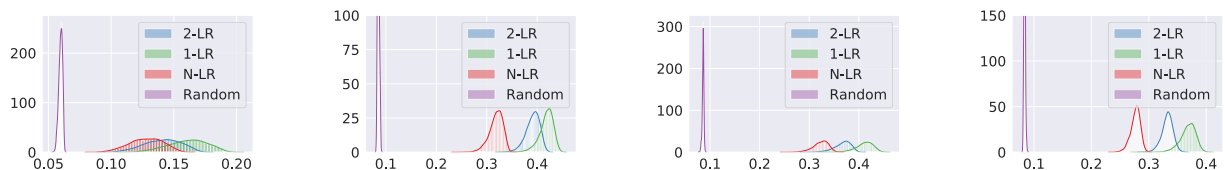


Figure 18: Cushion of Layer 2

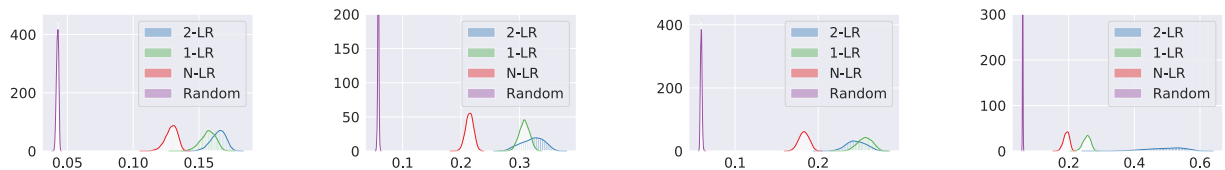


Figure 19: Cushion of Layer 3



Figure 20: Cushion of Layer 4